PROCEEDINGS OF SPIE

SPIEDigitalLibrary.org/conference-proceedings-of-spie

Mechanical design and thermal analysis of a 12U CubeSat MTCW lidar based optical measurement system for littoral ocean dynamics

Guentchev, George, Bayer, M. Mert, Li, Xun, Boyraz, Ozdal

George N. Guentchev, M. Mert Bayer, Xun Li, Ozdal Boyraz, "Mechanical design and thermal analysis of a 12U CubeSat MTCW lidar based optical measurement system for littoral ocean dynamics," Proc. SPIE 11832, CubeSats and SmallSats for Remote Sensing V, 118320B (17 August 2021); doi: 10.1117/12.2597709

SPIE.

Event: SPIE Optical Engineering + Applications, 2021, San Diego, California, United States

Downloaded From: https://www.spiedigitallibrary.org/conference-proceedings-of-spie on 03 Dec 2021 Terms of Use: https://www.spiedigitallibrary.org/terms-of-use

Mechanical Design and Thermal Analysis of a 12U CubeSat MTCW Lidar Based Optical Measurement System for Littoral Ocean Dynamics

George N. Guentchev*[a], M. Mert Bayer[a], Xun Li[a] & Ozdal Boyraz[a]
[a]Electrical Engineering and Computer Science Department, University of California, Irvine, CA92697, USA

ABSTRACT

In this work, we designed a 12U CubeSat (CS) Platform for a Multi-Tone Continuous Wave (MTCW) Lidar system, utilizing phase-based detection, which is used as optical altimetry and velocimetry measurement device. The spacecraft is designed to be operational for a period of 6 to 12 months, and the primary goals are to develop a standalone small spacecraft technology that enables an optical remote sensing system for littoral ocean dynamics including ocean surface height and wind vector measurements in the equatorial low earth orbit (LEO) with an altitude of 500 km. Here, we describe the mechanical design and the thermal analysis of the spacecraft. Due to the random vibration and shock response, related to the launching of the spacecraft, vibration isolation was designed to protect and preserve optical components and alignments, while meeting the dispensary system's maximum directional force requirements. Moreover, based on the necessity of high optical power, the pump and signal lasers were selected to operate at 975 nm and 1064 nm, respectively, with a total average optical power of 50W and a quasi-CW pulse peak power of 10 kW. As a result, the generated heat by the pump lasers creates thermally localized hot spots as much as 70 °C in the 12U CS that should be dissipated while remaining in the optimum operating temperature range of all components. Therefore, we designed thermal dissipation systems, including radiators, heat pipes, thermoelectric coolers, and used space-grade exterior paint to sustain the operation of the MTCW Lidar in the 12U CS.

Keywords: CubeSat, Lidar, Mechanical design, Modal Analysis, Random vibration analysis, Launch forces analysis, Thermal systems design, Thermal analysis

1. INTRODUCTION

The interest in small satellites, and particularly CubeSat platforms, has increased significantly in the past two decades [1]. The main contributing factors are the relatively low cost of CubeSat platforms and the rapid advance of technology that resulted in a significant price decrease and miniaturization of scientific components and subsystems. The relatively low cost and shorter development times of CubeSat platforms in comparison with the majority of the scientific satellites that are in use today have allowed universities and independent researchers to develop their space programs.

CubeSats come in different sizes ranging from 1U (or 1 unit), which measures 100mm x 100mm x 100mm and with a maximum mass of 2kg, to 12U, which measures 226mm x 226mm x 340.5mm and with a maximum mass of 24 kg, according to Cal Poly CubeSat Laboratory at Cal Poly, San Luis Obispo guidelines [2]. However, different dispensary system manufacturers have their specifications for the payloads and some even offer 16U bus options [3]. The small size and the limited radiating surface area of the CubeSat platforms, however, offer significant challenges in terms of mechanical design and thermal management. The classical approach of mounting discrete components to a pre-build satellite body leads to a larger size and difficult thermal control. In order to solve the challenges of limited payload volume, thermal management, vibration, and shock response, our team developed an integrated CubeSat Lidar system that incorporates the optical and laser components along with the satellite support subsystems in the body of a 12U CubeSat platform. The innovative satellite design integrates components mounting brackets and body parts as structural support and thermal path to the exterior radiating surfaces. Another novelty in the design is the optical systems bracket and its shock protection design.

In this work, we show the design and analysis of the 12U CubeSat Phase-Based Multi-Tone Continuous Wave Lidar Optical Measurement System in Low Earth Orbit (LEO) of 500km that is planned to operate for a mission duration of 12 months as illustrated in Figure 1. The CubeSat design process addresses the Planetary Systems Corporation 12U Dispensed

CubeSats and SmallSats for Remote Sensing V, edited by Thomas S. Pagano, Charles D. Norton, Sachidananda R. Babu, Proc. of SPIE Vol. 11832, 118320B
© 2021 SPIE · CCC code: 0277-786X/21/$21 · doi: 10.1117/12.2597709

Downloaded From: https://www.spiedigitallibrary.org/conference-proceedings-of-spie on 03 Dec 2021
Terms of Use: https://www.spiedigitallibrary.org/terms-of-use

System requirements and the NASA General Environmental Verification Standard (GEVS) for spacecraft 45.4-kg (100-lb) or less. The mechanical design is performed using SolidWorks, the random vibration and stress analysis for launch conditions is performed using SolidWorks Simulation, thermal analysis is performed using SolidWorks Flow Simulation, and the solar flux calculations are performed using MATLAB.

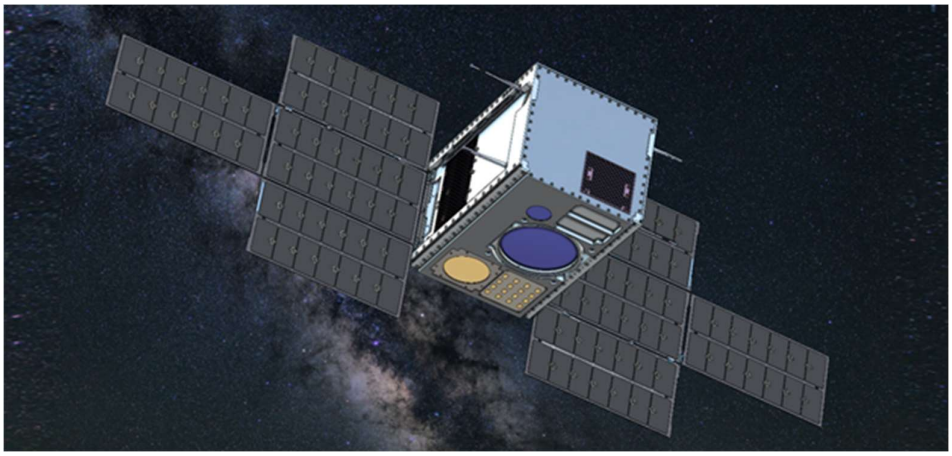

Figure 1. 12U CubeSat MTCW Lidar Based Optical Measurement System

The Planetary System Corporation (PSC) Canisterized Satellite Dispenser is the dispenser system chosen for this design as depicted in Figure 2. One of the main reasons is that it features preloaded payload tabs, which create a predictable load path to the payload, so stress at critical locations like fast-steering mirrors and reaction wheel bearings can be accurately calculated. The preloaded tabs also allow for engineering a design that protects the sensitive components. The dispenser also features a separation electrical connector that allows communication and charging between payload and launch vehicle prior to and during launch. The dispenser-constrained deployable greatly reduce the costs and complexity of payload modules like solar panels and antennas. The dispenser has the largest volume versus existing designs and accommodates larger payloads that have 15% more volume and can be 2.5cm longer than standard CubeSats with payload dimensions measuring 229mm x 239mm x 366mm [4].

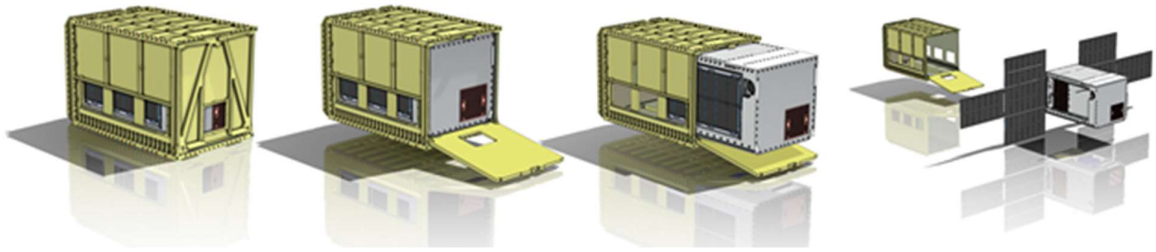

Figure 2. The Planetary System Corporation Canisterized Satellite Dispenser

2. OPTICAL MEASUREMENT SYSTEM FOR LITTORAL OCEAN DYNAMICS

2. 1. Optical Specifications

The CubeSat-based Optical Measurement System for Littoral Ocean Dynamics mission is a joint project between the University of California, Irvine's (UCI) Advanced Photonic Devices and Systems Laboratory (APDSL), and Jet Propulsion Laboratory (JPL) funded by the Office of Naval Research (ONR). The main objective is to develop a standalone small spacecraft technology that enables an optical remote sensing system using a Phase-Based Multi-Tone Continuous Wave laser system (PB-MTCW) for littoral ocean dynamics such as ocean surface height and wind vector. The mission requires accurate (1m/s) wind measurements within the desired resolution regime and accurate (<4cm) ocean surface height measurements. Also, the maximum amount of possible areal coverage (>2%) with an achievable lateral resolution with

Downloaded From: https://www.spiedigitallibrary.org/conference-proceedings-of-spie on 03 Dec 2021
Terms of Use: https://www.spiedigitallibrary.org/terms-of-use

30m spot size on the ocean surface and pointing accuracy of ± 26.2m (0.003°). Moreover, the satellite needs to complete the data transmission in each orbit that limits the amount of generated data and the duration of onboard data processing. The targeted scanning pattern is illustrated in Figure 3.

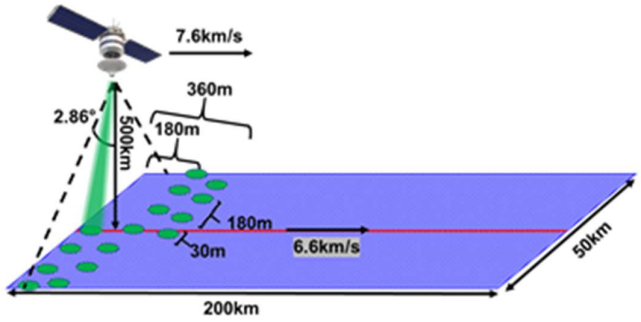

Figure 3. Illustration of the targeted scanning pattern to cover a 200km x 50km area on the ocean for optical remote sensing.

To achieve the mission requirements, first, the optical parameters are determined. The calculated parameters are tabulated in Table 1. For long-distance optical remote sensing, the optical power requirements are very strict. In our design, the targeted optical average power is 50W. By applying a modulation with a duty cycle of 0.5%, a quasi-CW pulse can be realized with a peak power of ~10kW. This power can generate results up to 10dB signal-to-noise ratio(SNR) after considering potential scattering and optical losses. However, utilization of such high optical powers exhibits a crucial need for thermal management, as well.

Table 1. Optical design parameters to satisfy mission requirements

Parameters	Value
Coverage angle	±2.86°
Repetition rate	10kHz
Resolution in swath	~180m
Total number of data points	303,020
Total coverage percentage	~2.14%
Scanning mirror speed	18.33Hz
Total scan duration	~40s
Average optical power	~50W
Time window per measurement	500ns
Frequency resolution (speed resolution)	2MHz (1m/s)
Duty cycle of quasi-CW pulse	0.5%
Pulse peak power	~10kW

2. 2. Phase-Based Multi-Tone Continuous Wave Lidar

PB-MTCW Lidar is a different ranging and velocimetry approach compared to other continuous-wave (CW) Lidar alternatives that utilize coherent ranging techniques. In PB-MTCW, we modulate a CW laser signal with multiple radio-frequencies (RF) through a Mach-Zehnder Modulator (MZM) to realize optical sidebands near the main carrier frequency. [5.6] A fraction of the unmodulated CW signal is kept as a local oscillator to boost the echo signal power. Each RF tone on the optical carrier accumulates a different phase with respect to its frequency and total covered propagation distance.

Downloaded From: https://www.spiedigitallibrary.org/conference-proceedings-of-spie on 03 Dec 2021
Terms of Use: https://www.spiedigitallibrary.org/terms-of-use

By analyzing the relative phase and frequency differences between each sideband, it is possible to extract the range of the target [7]. On the other hand, the Doppler shifts induced to the optical carrier paves the way to achieve velocimetry, as well. In summary, the PB-MTCW Lidar enables the CubeSat system to perform remote optical altimetry and velocimetry [8,9] with single-shot results by eliminating any form of phase, frequency, or amplitude sweeping compared to the other CW alternatives [10].

2. 3. Laser Subsystem

The schematic of the designed laser subsystem is presented in Figure 4(a). The primary goal of this design is to achieve a low-noise amplified optical signal at the output of the collimator (CL). The laser system utilizes a 1064 laser diode from OE Waves (HI-Q) with a <100Hz linewidth, two Pre-Amplifiers from Cybel (Mako-Amp1064), two modulators (High-Speed iXblue NIR-MX-LN (MZM) and low-speed G&H T-M200-0.1C2G-3-F2S (AOM)), two pump lasers (CNI Laser LDM-976-70-CK), two pump laser drivers (Maiman Electronics SF6060), four Wavelength Division Multiplexers, six monitoring photodetectors, and the main balanced photodetector (Thorlabs PDB482C-AC). The laser components are contained in the laser components assembly to prevent any impact of the vibration on the fiber optics.

The first MZM is used to compensate for the constant speed realized by the CubeSat due to its orbital motion. This motion yields a constant Doppler shift and should be attributed to realizing coherent ranging. The phase-locked RF generators are combined and fed to the second MZM for modulation of the CW laser that creates the sidebands. The quasi-CW pulsation is achieved through a high extinction-ratio acousto optic modulator to realize high peak powers. The preamplifiers are implemented with fiber-Bragg-grating (FBG) to realize low-noise amplification before the actual amplification through YDF and pump lasers. The expected average optical output power of the system is 62W, while two pump lasers operate at 75W optical power. The simulated output spectrum is given in Figure 4(b). The pump and signal lasers will operate for 90s at each orbit that includes the stabilization and data acquisition times.

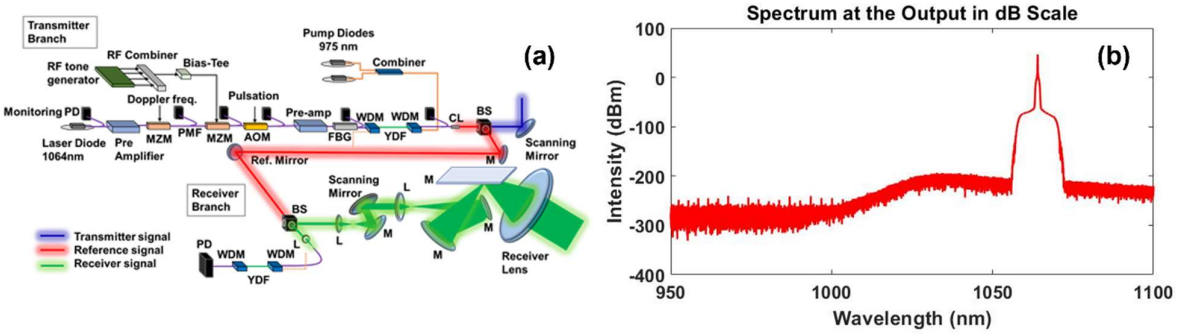

Figure 4. (a) Schematic of laser subsystem to realize PB-MTCW Lidar. (b) Simulation of the expected output signal.

3. MECHANICAL DESIGN

The main challenges to the design of the 12U CubeSat MTCW Lidar Based Optical Measurement System were the limited space, random vibration response, and thermal management. The spacecraft is designed according to 12U geometry following the Planetary Systems Corporation guidelines for their 12U Dispenser System and all requirements were satisfied. Aluminum 7075-T651 is used for the design of all aluminum components unless specified otherwise and the radiators/heat sinks are made from copper. The aluminum and copper need to undergo an oxidation process before the assembly. The design utilizes silicone rubber shock absorbers to protect the optical system assembly from shock and vibration during launch. The shock absorbers need to undergo ten hours of the heat treatment process at 204 ºC to prevent outgassing during the mission. The bottom plate is designed to act as a shock absorber to further reduce the effects of the launch. Every component is brought to the software environment according to their datasheets. The satellite's total estimated mass is 23.65 kg. A list of each component used for the assembly is given in Table 2 with their corresponding mass for total weight estimation.

The satellite consists of eight main assemblies. The whole satellite structural support, however, is contained within multiple assemblies, including the satellite body panels, laser components assembly brackets, and optical system brackets. To fit the design in a 12U bus, the laser components brackets also act as the batteries brackets and provide structural

Downloaded From: https://www.spiedigitallibrary.org/conference-proceedings-of-spie on 03 Dec 2021
Terms of Use: https://www.spiedigitallibrary.org/terms-of-use

support along with the satellite body plates. Integrating the mounting brackets into the satellite structural support was the only approach that could provide enough space for the optical assembly. With the integration approach, the design was able to satisfy the vibration and shock requirements on one hand and provide a thermal path from interior components to exterior radiating surfaces on the other. These assemblies are illustrated in Figure 5 with an exploded view of the CubeSat.

Table 2. Weight estimation of the satellite based on the used components.

Module/Part Name			Mass (kg)	
Assembly	Parts	Quantity Used	Individual	Total
	Optics	1	0.486	0.486
	Collimator	1	0.5	0.5
Transmitter	Bracket			0
	Optics	1	1	1
Reciever	Bracket			0
Electronics Boards	Circuit Boards	1	1	1
	Case	1	1.2	1.2
Battery Module	Pumpkin Lithium Battery Modu	4	0.71	2.84
	XACT100 Control Module	1	0.433	0.433
	Star Tracker	1	0.35	0.35
Attitude Control Module	Reaction Wheel	3	0.345	1.035
	HaWK 17AS56	2	0.31	0.62
Solar Panels	SADA Module	1	0.25	0.25
Cables	Multiple	1	1	1
Signal Laser	OE Waves	1	0.25	0.25
Pre-Amps	MAKO-AMP1064	2	0.2	0.4
Pump Laser	CNI- Pump LDM-976-70-CK	2	0.1	0.2
WDM	DK Photonics 2x1	4	0.05	0.2
AOM	Gooch & Housego FIBER-Q	1	0.1	0.1
RF Signal Generator	Custom	1	0.05	0.05
RF Combiner	Custom	1	0.1	0.1
RF Bias Tee	Custom	1	0.05	0.05
MZM	IXBlue NIR-MX-LN series	2	0.1	0.2
Hardware	Misc.	1	1	1
Comm Module	Xlink Xband Transceiver	1	0.2	0.2
Satellite Body	Bottom Plate	1	0.95194	0.95194
	Back Plate	1	0.618	0.618
	Left Plate	1	0.529	0.529
	Right Plate	1	0.54	0.54
	Top Plate	1	0.53	0.53
	Top Cover Panel	1	0.2	0.2
	Front Cover Panel	1	0.237	0.237
	Telescope Bracket Receiver	1	1.55	1.55
	Telescope Bracket Transmitter	1	1.05	0.977
	Laser Components Assembly	1	1.5	1.5
		Tot. Body	7.70594	
Battery Bracket				0
Radiators		2	1.274	2.548
Total Mass (kg)				23.64494

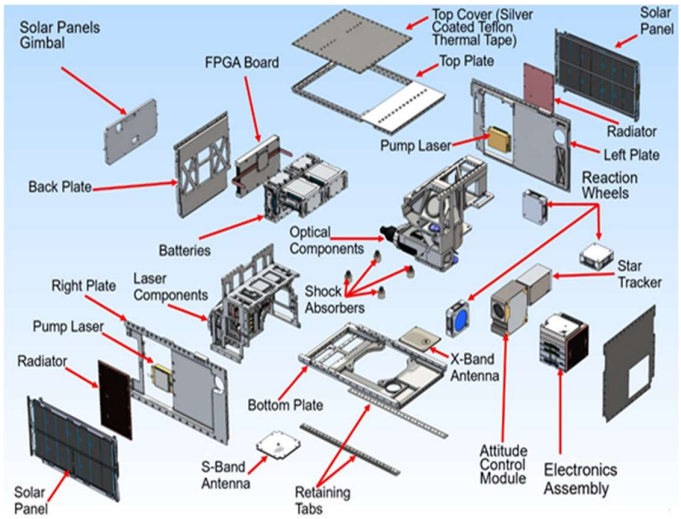

Figure 5. CubeSat exploded view indicating the subsystems and assembly units.

Downloaded From: https://www.spiedigitallibrary.org/conference-proceedings-of-spie on 03 Dec 2021
Terms of Use: https://www.spiedigitallibrary.org/terms-of-use

3. 1. Satellite Body

The satellite body consists of the bottom plate, side plates, backplate, top plate, top and front covers, and the integrated laser components mounting brackets. It provides mounting for the solar panels, solar panels gimbal, communication antennas, and radiators. All components (except the shock absorbers) are made from 7075-T651 aluminum alloy. The machined parts need to undergo a high-temperature oxidation process before assembly. The fasteners in the design are made from Series C300 corrosion-resistant (CRES) stainless steel. Figure 6 shows the side view of the designed CubeSat and the optical assembly.

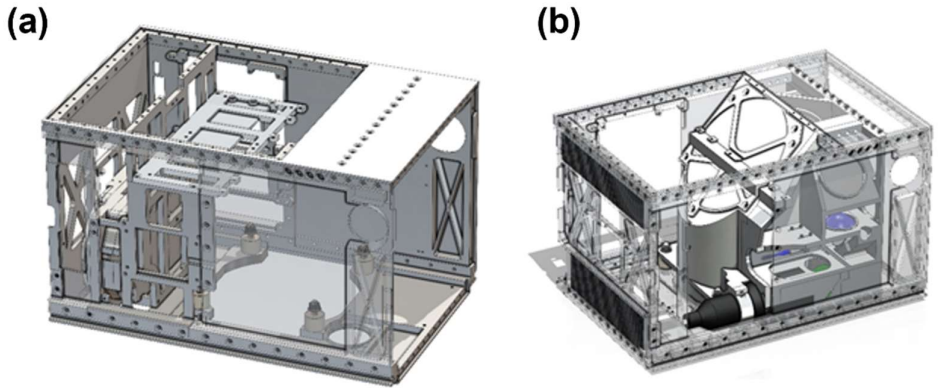

Figure 6. (a) Side view of the satellite body. (b) Side view emphasizing the optical assembly subsystem

The bottom plate utilizes a unique design that makes it act as an element in a suspension system for the optical assembly as illustrated in Figure 7. If simplified, the structure would resemble two longitudinal bars connected with series of transverse bars. The longitudinal bars serve as mounting structures for the retaining tabs and the side plates. If the tabs experience a shock event, the energy is transferred to the bottom plate, and the transverse bars bend, resembling a leaf suspension system. This effectively acts as a buffer that stores the shock energy and releases it slowly, reducing the effects transferred to the rest of the system. The optical assembly is connected to the bottom plate via silicone rubber shock absorbers, further reducing the acceleration at critical system components.

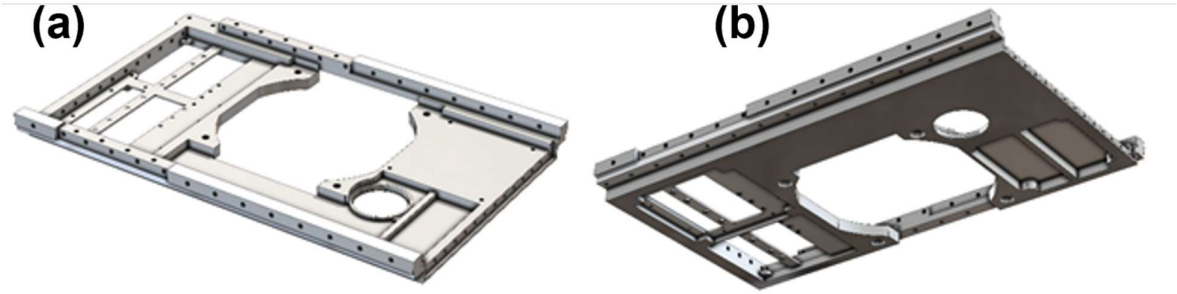

Figure 7. Bottom plate design (a)interior side, (b) exterior side.

In addition, the backplate is machined to incorporate the radiators for the FPGA and the Pre-Amplifiers and provide mounting for the solar panels' gimbal. The backplate also acts as structural support and it is mounted to the bottom plate, side plates, and top plate. The radiators' effectiveness is significantly reduced in vacuum conditions, however, the FPGA temperature decreased by 4 ºC in comparison with the design that didn't utilize radiators. The rear view of the backplate is given in Figure 8, along with the view of the backplate with gimbal and the deployed solar panels. Moreover, the side plates provide the satellite body with structural support and provide housing space and mounting for the stowed solar panels and their release mechanism. The side plates also provide mounting for the side radiators. Both side plates feature openings for the attitude control module and the star tracker which are indicated in Figure 9(a-b). Similarly, the top plate acts as a mounting bracket for the optical systems assembly to attach to the satellite body. They are connected via eight M6 bolts that provide a stiff connection. This ensures that no misalignment occurs between the satellite body and the

Downloaded From: https://www.spiedigitallibrary.org/conference-proceedings-of-spie on 03 Dec 2021
Terms of Use: https://www.spiedigitallibrary.org/terms-of-use

optical systems assembly during launch. The bottom plate contains the communication antennas and misalignments could lead to communication system issues. The top plate itself was not taped with the silver-coated Teflon thermal tape to avoid dropping below the min operating range of system components as shown in Figure 9(c-d).

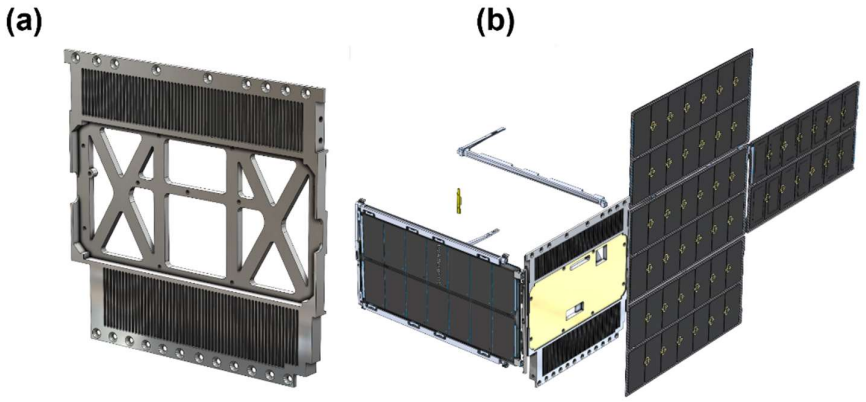

Figure 8. (a) Backplate rear view without the gimbal. (b) Backplate with mounted solar panels which are stowed and deployed along with gimbal

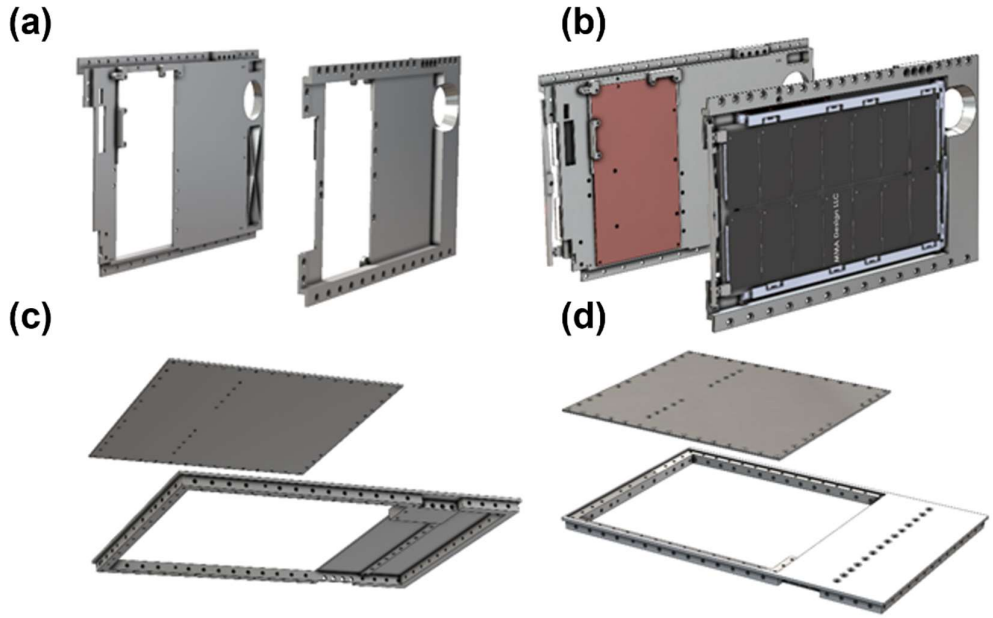

Figure 9. (a-b) Side plates with and without radiators and solar panels, respectively. (c-d) Interior and exterior view of the top plate, respectively.

The front and the top cover panels provide some structural support, isolate the satellite interior, and serve as reflective surfaces to reject some of the sun's radiation. They are both covered with silver-coated Teflon thermal tape which is used for passive thermal control. They are recessed by 2mm from the outer surfaces of the satellite in order to accommodate the tape. The cover panels are 2mm thick and are also made of 7075-T651 aluminum alloy. The cover plates are indicated on the satellite body in Figure 10(a).

Downloaded From: https://www.spiedigitallibrary.org/conference-proceedings-of-spie on 03 Dec 2021
Terms of Use: https://www.spiedigitallibrary.org/terms-of-use

3. 2. Optical Receiver Assembly

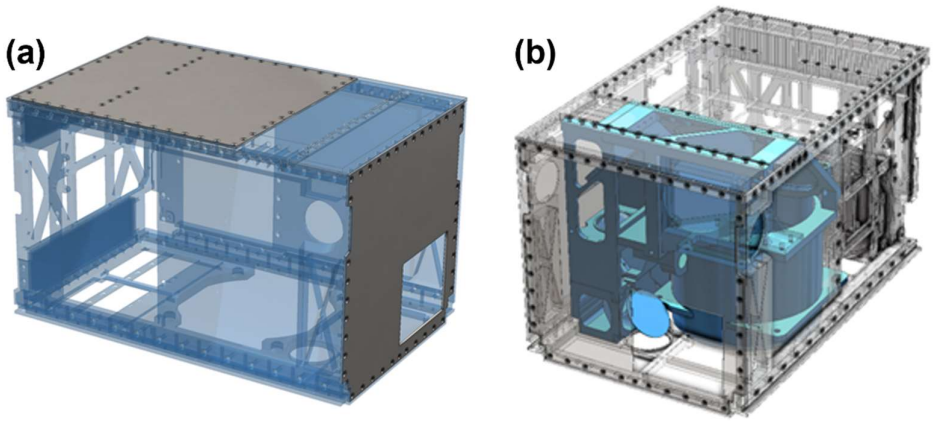

Figure 10. (a) Top and front cover panels on the CubeSat body. (b) Optical system assembly inside the CubeSat.

The optical assembly contains the transmitter and receiver branch optical components and the fast-steering mirrors and its position within the design is illustrated in Figure 10(b). To protect the design from shock, it is mounted on four silicone shock absorbers to the bottom plate and eight M6 bolts to the upper plate. The sturdy connection at the top ensures that the alignment with the rest of the satellite body is not compromised during launch. The alignment between the attitude control system and the optical system assembly is crucial so the exact location of the laser spot on the ground is known. The integration of the attitude control module is presented in Figure 11. In order to prevent misalignment between the two systems, the attitude control system is mounted directly to the optical assembly brackets. To address the outgassing of silicone rubber in a vacuum pretreatment of 10 hours at 204 ºC would remove the majority of volatile compounds [11] and make the silicone rubber fit for use in LEO environment.

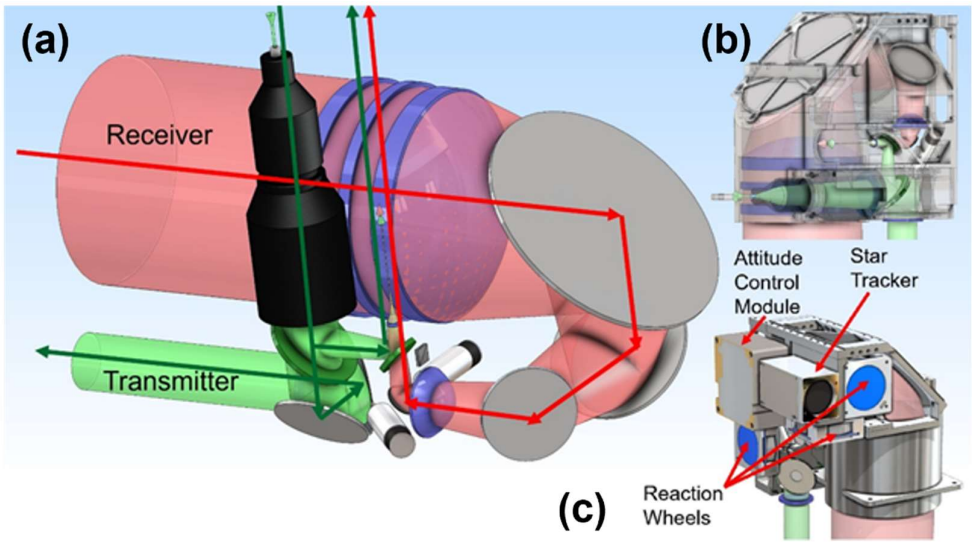

Figure 11. (a) Receiver and transmitter optical path. (b) The optical path inside the optical bracket. (c) The attitude control system is mounted to the receiver optics assembly.

The optical brackets allow adjustment of all the lenses and mirrors through using cylindrical lens holders and spacers. The retainers and assembly allowing the positioning of the lenses are illustrated in Figure 12. The lens holders have the same diameter and need to be precision machined to fit into the main receiver optical bracket cavity. The thickness of the spacers between the lens holders can be changed to accommodate lens adjustments so that system can be optimized.

Downloaded From: https://www.spiedigitallibrary.org/conference-proceedings-of-spie on 03 Dec 2021
Terms of Use: https://www.spiedigitallibrary.org/terms-of-use

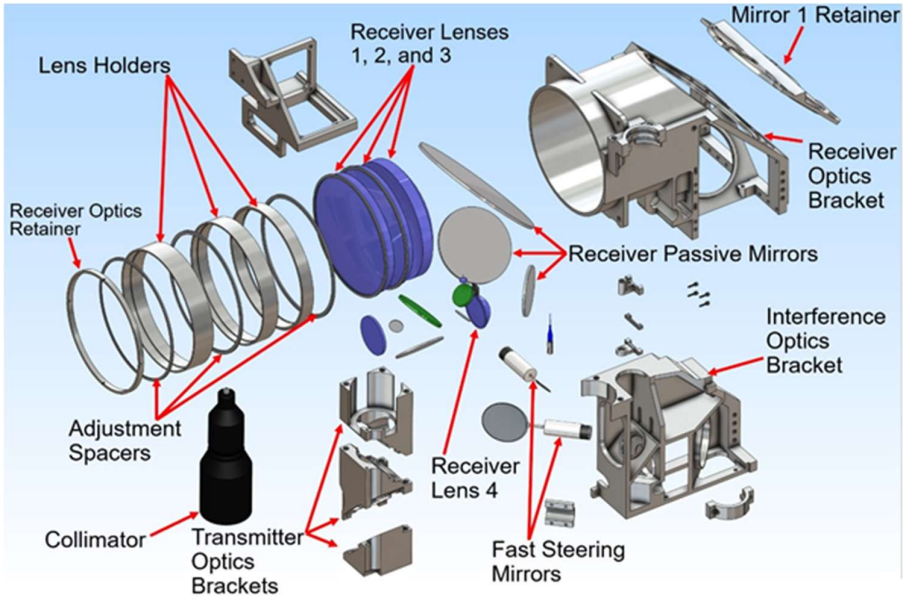

Figure 12. Optical receiver assembly exploded view indicating the individual components.

The receiver branch contains three custom 135 mm lenses followed by three flat mirrors, used to fold the optical path to fit the optical assembly in the limited space of the CubeSat as illustrated in Figure 13. The three 135 mm lenses allow adjustment of ±2 mm along the optical axis. The optical brackets allow adjustment of the mirrors ±1 mm along their axis to achieve optimal fiber coupling. After the fixed mirrors there is a 40 mm lens followed by the receiver fast-steering mirror. The 40mm lens is also adjustable with a ±1 mm range along the optical axis, however, the fast-steering mirror is fixed in the receiver optical bracket and all adjustments need to be done around it. Following is the beam splitter that interferes with the transmitter and receiver beams. The last component is a two custom lens collimator and the fiber leading to the photodetector.

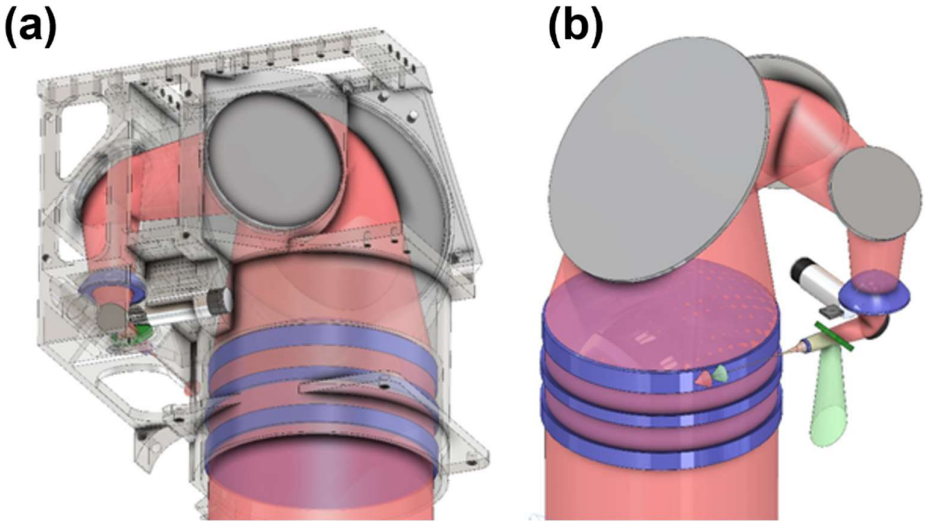

Figure 13. (a) Receiver assembly beam path inside the optical bracket. (b) Receiver optics assembly.

Downloaded From: https://www.spiedigitallibrary.org/conference-proceedings-of-spie on 03 Dec 2021
Terms of Use: https://www.spiedigitallibrary.org/terms-of-use

3. 3. Optical Transmitter Assembly

The transmitter branch consists of the collimator assembly, beam splitter, fixed output mirror, output fast-steering mirror, and mounting brackets. The collimator bracket, beam splitter bracket, and fixed output mirror bracket provide a unique optics mounting design that allows the maximum output beam diameter as illustrated in Figure 14. Traditional designs use a threaded retaining ring that would block a portion of the laser beam so a larger diameter beam splitter and mirrors would need to be used. The fast-steering mirror is mounted on the interference bracket, which is shared by the receiver and transmitter branches. The alignment between the brackets is ensured through the use of guiding pins.

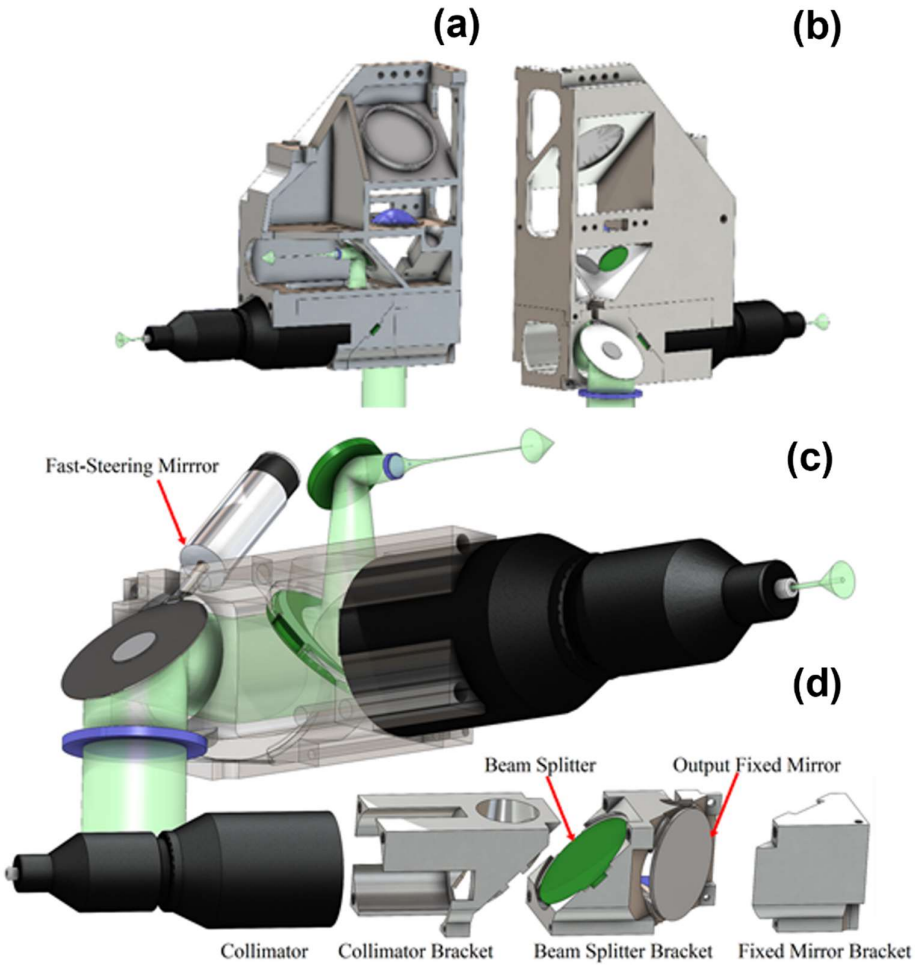

Figure 14. Optical transmitter assembly (a) front view, (b) rearview. (c) Beam path in the transmitter branch. (d) Exploded view of the transmitter branch brackets.

3. 4. Laser Assembly

The laser components assembly serves multiple functions in this design. The material used for the structure is 7075-T651 Aluminum alloy like the rest of the satellite body. It contains all the laser system components that are connected to optical fiber and provides a thermal path to the exterior radiating surfaces. The design incorporates a fiber routing board that protects the optical fibers from excessive bending and houses the combiners/splitters. It features openings that allow optical fiber to pass through and reach the necessary components and the fiber channel design allows any length of optical fiber to be secured. Figure 15 indicates the laser assembly components with an exploded view. Similarly, the route for fiber optics is provided in Figure 16. The routing board along with the rear caps provide a safe structure that prevents damage to the delicate optics.

Downloaded From: https://www.spiedigitallibrary.org/conference-proceedings-of-spie on 03 Dec 2021
Terms of Use: https://www.spiedigitallibrary.org/terms-of-use

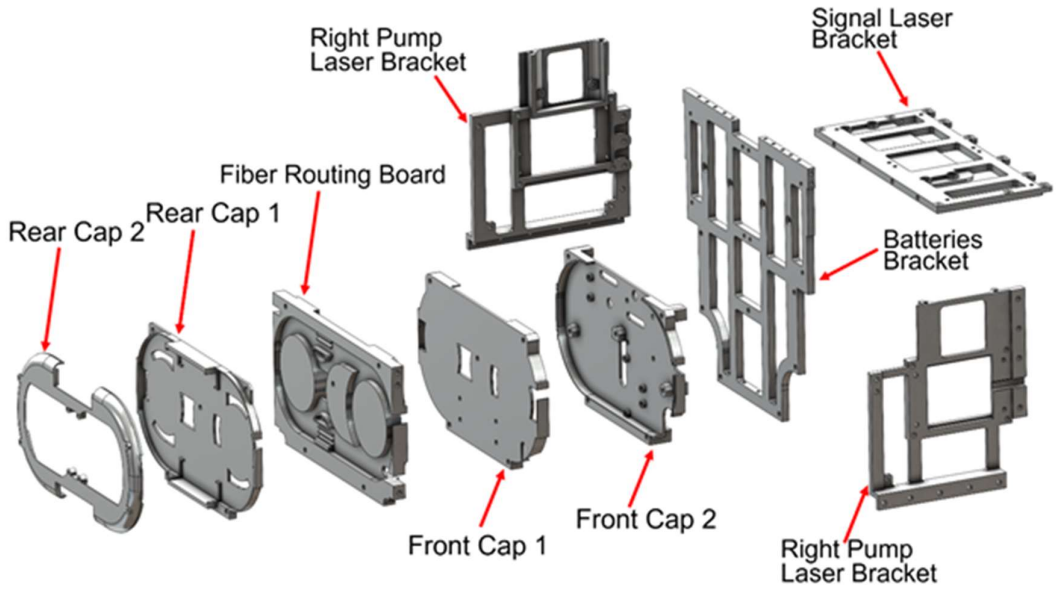

Figure 15. Laser components assembly structural components exploded view.

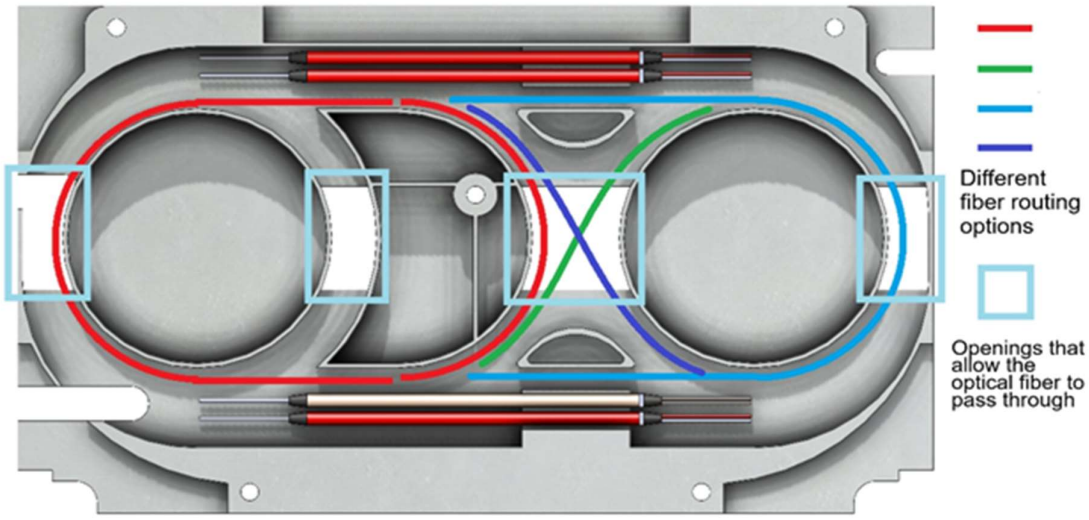

Figure 16. Laser assembly fiber routing board.

The pump laser brackets house the pump lasers and the Thermoelectric cooler (TECs). The side radiators, which also serve as heat sinks, are mounted to the pump laser brackets as well. When they are tightened, the TECs are sandwiched between the pump lasers and the radiators, ensuring optimal heat exchange between them. The signal laser features an integrated TEC, so its mounting bracket, along with a heat pipe, leads the excess heat to the radiators. The structure also serves as a mounting bracket for the batteries along with the Batteries bracket. It is possible to visualize these properties in Figure 17. Similarly, heat pipes are used for the FPGA and the signal laser for thermal control, as well.

Downloaded From: https://www.spiedigitallibrary.org/conference-proceedings-of-spie on 03 Dec 2021
Terms of Use: https://www.spiedigitallibrary.org/terms-of-use

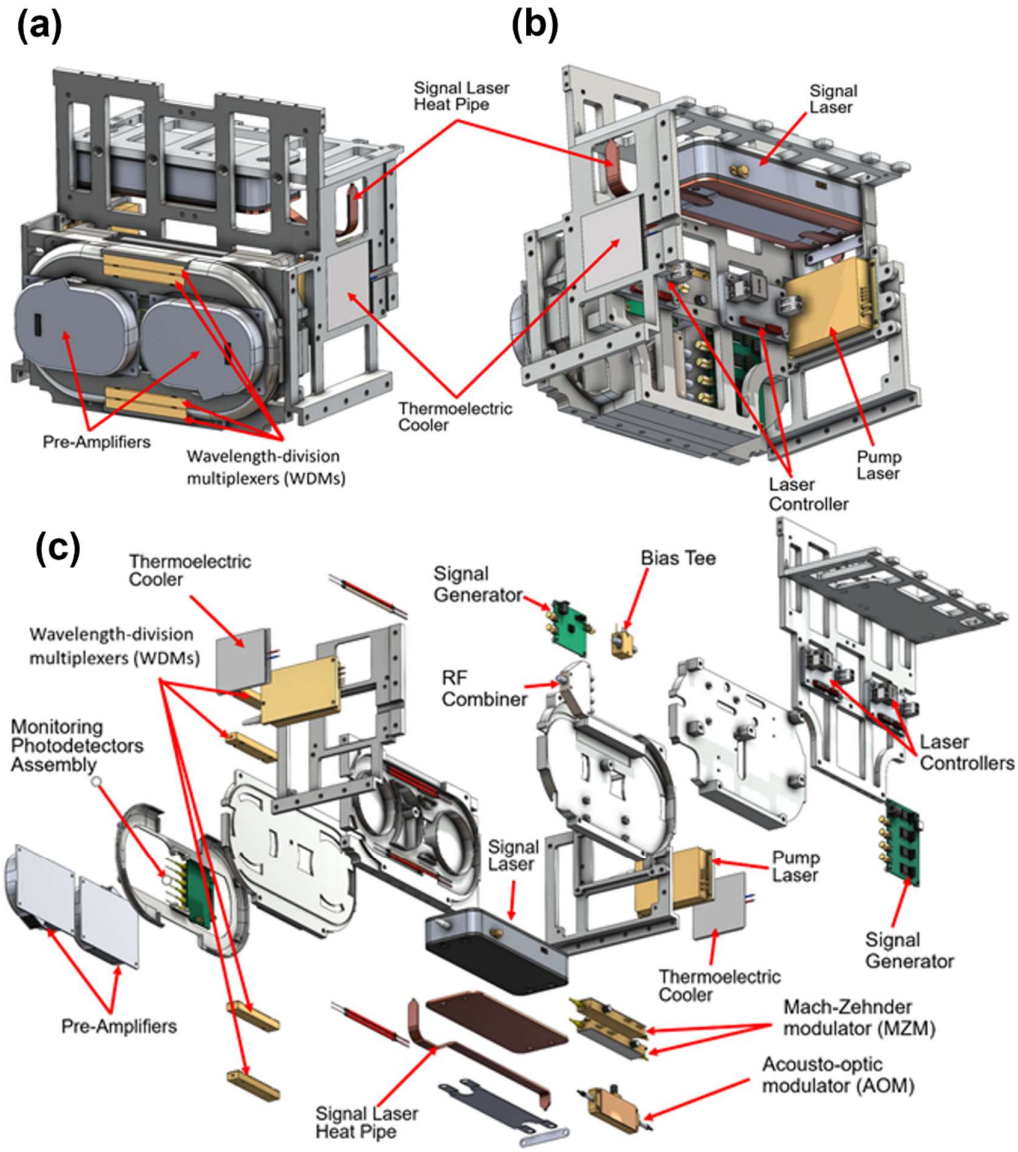

Figure 17. Complete laser assembly (a) front view, (b) rearview. (c) The exploded view of the laser assembly.

3. 5. Attitude Control Subsystem

The attitude control system consists of Blue Canyon XACT-100 attitude control module, Blue Canyon NST star tracker, and three Blue Canyon RWP100 reaction wheels. The XACT-100 system provides ±0.003 deg (1-sigma) for 2 axes and ±0.007 deg (1-sigma) for the 3rd axis, however, with the addition of the star tracker it can provide ±0.003 deg (1-sigma) for all three axes. The alignment between the optical system and the attitude control module is critical because that ensures the correct location of the laser beam on the ground and because of that the attitude control system components are attached to the optical systems assembly. This way the alignment between the two systems would be protected during launch and the sensitive reaction wheel bearings would be protected from shock. The position of the attitude control subsystem inside the satellite along with the individual control modules is indicated in Figure 18.

Downloaded From: https://www.spiedigitallibrary.org/conference-proceedings-of-spie on 03 Dec 2021
Terms of Use: https://www.spiedigitallibrary.org/terms-of-use

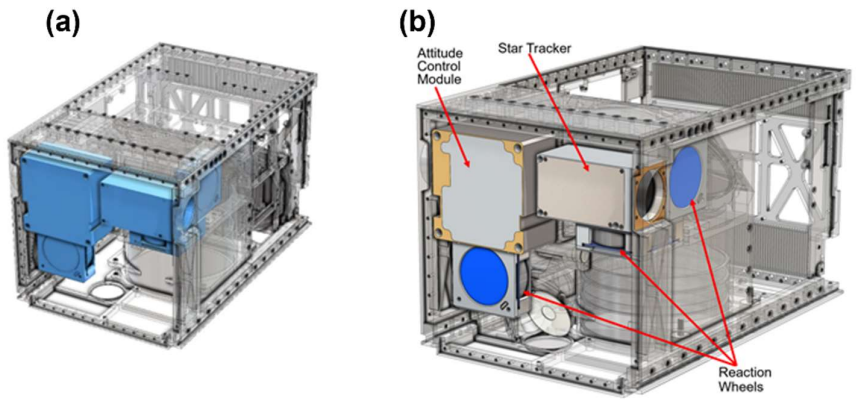

Figure 18. (a) Attitude control subsystem position within the CubeSat. (b) Attitude control subsystem modules.

3. 6. Control Electronics Assembly and Communication Subsystem

The electronics assembly houses the onboard computer, the motherboard, the mirror control boards, and the communication modules, which are depicted in Figure 19(a). The case is custom-designed to contact the heat-producing elements, such as microchips. Vacuum thermal grease will have to be used to prevent outgassing and offer good thermal conductivity to the case. It also features a heat sink/radiator that helps regulate the temperature during high power regimes, such as data transmission.

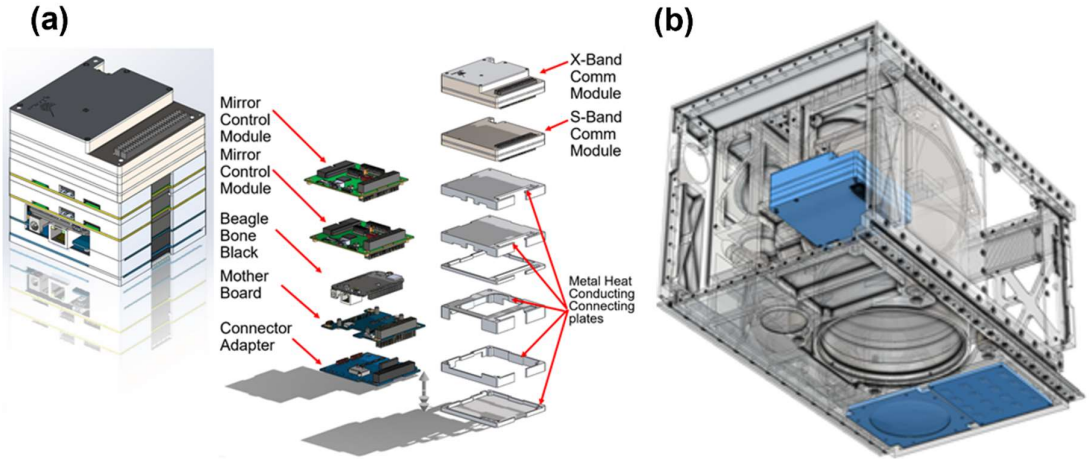

Figure 19. (a) Exploded view of the electronics assembly. (b) Position of the electronics assembly along with the X-Band and S-band antenna establishing the communication subsystem.

The communication systems consist of Endurosat X-Band and S-Band communication modules and the Endurosat X-Band and S-Band antennas mounted on the bottom plate. The communication modules are part of the electronics assembly because they need the OBC connection and they are designed for the standard size used by the Pumpkin Space OBC module. It is possible to visualize the position of the X-Band and S-Band antenna on the CubeSat as in Figure 19(b).

3. 7. FPGA Assembly

The FPGA Board Assembly consists of the Virtex 5 FPGA board, custom case, heat pipe that leads to the side radiators, and a heat pipe retainer. Inside the CubeSat, the FPGA is directly bolted to the backplate, which has a radiator machined in it. FPGA is heavily utilized for data processing and data compression before transferring the data to the ground unit through the communication subsystem. The heat dissipation during this process is marginally high. The heat pipe used is Advanced Thermal Solutions ATS-HP-F4L300S8W-183 and it is clamped to the FPGA board to prevent heat accumulation over the FPGA board. The assembly of heat pipes and FPGA is illustrated in Figure 20(b).

Downloaded From: https://www.spiedigitallibrary.org/conference-proceedings-of-spie on 03 Dec 2021
Terms of Use: https://www.spiedigitallibrary.org/terms-of-use

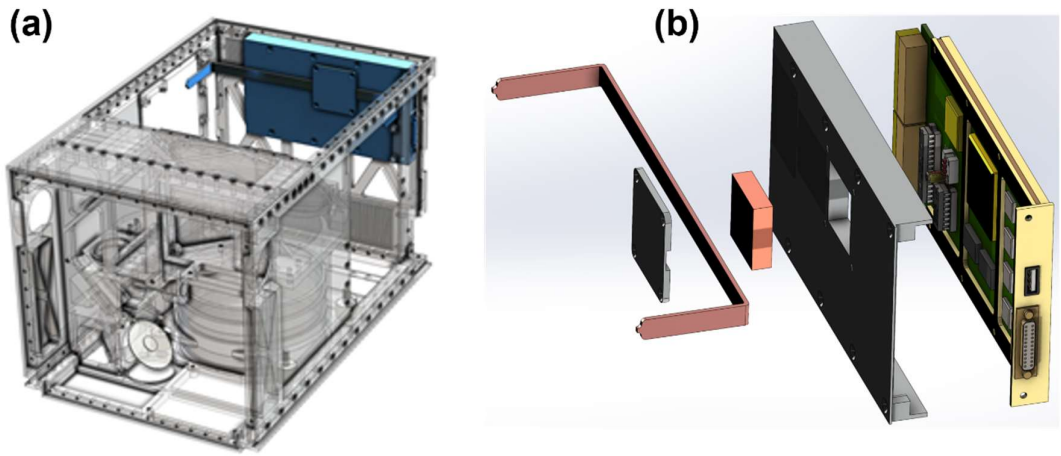

Figure 20. (a) Position of the FPGA module in the CubeSat. (b) Exploded view of the FPGA module.

3. 8. Power subsystem

The power systems consist of two MMA Design eHAWK 27AS112 solar panels, the MMA Design 2U gimbal system, and four Pumpkin Space Intelligent Protected Lithium Battery Modules with state of charge reporting (BM2). Three of these units are working in parallel to achieve a total capacity of 240Wh and provides current up to 45A. Two power buses operate at 12V and 5V. One of the lines powers up to power-hungry lasers and FPGA, while the other powers the remaining electronics. The gimbal is mounted to the backplate. The side plates contain the solar panel release mechanism and hold the solar panels when stowed. The four batteries are mounted to the laser components assembly. The power subsystem units are indicated in Figure 21.

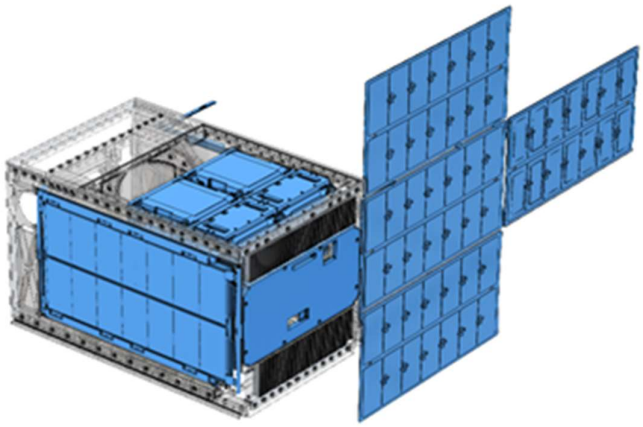

Figure 21. Power subsystem units.

4. SIMULATION RESULTS AND ANALYSIS

4.1. Vibration Analysis

In order to test compliance with NASA's guidelines and PSC's Canisterized Satellite Dispenser (CSD) guidelines, a simplified model of the payload was created, consisting of the primary structure and significant components for a Normal Modes Analysis from 20-2,000Hz [12]. Second, the dominant resonant frequencies were identified and mode shapes for each orthogonal direction (X, Y, Z). These modes can be identified as having the highest percentage of Modal Effective Mass relative to all modes modeled within the frequency bandwidth stated above.

Downloaded From: https://www.spiedigitallibrary.org/conference-proceedings-of-spie on 03 Dec 2021
Terms of Use: https://www.spiedigitallibrary.org/terms-of-use

The motivation behind the choice of Planetary System Corporation's Dispensary System is their use of preloaded payload tabs, which create a predictable load path to the payload, so stress at critical locations like fast-steering mirrors and reaction wheel bearings can be accurately calculated. The tabs allow to predict and design a shock and vibration path that dampens the response while maintaining the alignment of optical components and sensitive electronic components.

The previous version of the design needed improvement in the isolation of the optical component and the fast-steering mirrors. The design didn't fail any of the qualification requirements, however, strain affected multiple locations in the design. To address these issues the new design utilized an innovative mounting of the optical systems assembly. It rests on four silicone rubber shock absorbers and it has a solid connection with the top plate ensured by eight main M6 Series C300 corrosion-resistant (CRES) stainless steel fasteners and fourteen M4 fasteners made from the same material. The bottom plate also acts as a shock-absorbing element. It utilizes a design that contains two longitudinal bars connected with a series of transverse bars, which act as a suspension element. The side plates also reduce the shock response before it reaches the top plate, which provides a solid connection of the optical systems assembly to the rest of the body. The idea behind the design can be seen in Figure 22.

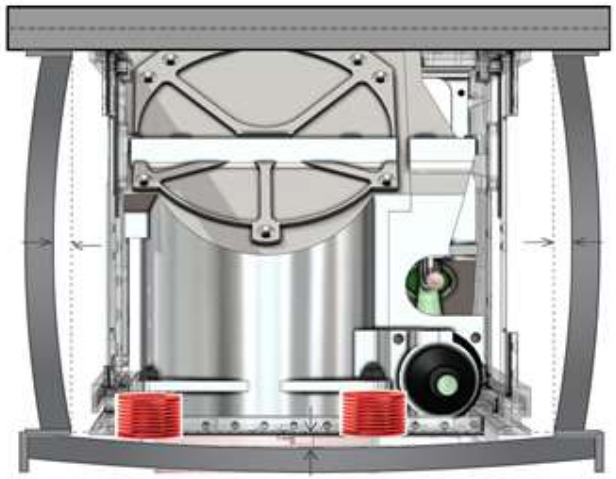

Figure 22. Exaggerated defects of the bottom plate, side plates, and shock absorbers.

4. 1. a Methodology

Frequency modal simulation, random vibration simulation, and launch forces simulations were performed. The modal analysis helps identify the dominant mode in all directions and determine the cumulative effective mass participation factor. The random vibration simulation is performed following NASA's General Environmental Verification Standard (GEVS) for spacecraft 100 lbs or less [13]. A brief summary of the standards is presented in Figure 23.

The plateau acceleration spectral density level (ASD) may be reduced for components weighing between 45.4 and 182 kg, or 100 and 400 pounds according to the component weight (W) up to a maximum of 6 dB as follows:

	Weight in kg	Weight in lb
dB reduction	= 10 log(W/45.4)	10 log(W/100)
$ASD_{(plateau)}$ level	= 0.04•(45.4/W)	0.04•(100/W)

The sloped portions of the spectrum shall be maintained at plus and minus 3 dB/oct. Therefore, the lower and upper break points, or frequencies at the ends of the plateau become:

F_L = 80 (45.4/W) [kg] = 80 (100/W) [lb] — F_L = frequency break point low end of plateau

F_H = 500 (W/45.4) [kg] = 500 (W/100) [lb] — F_H = frequency break point high end of plateau

The test spectrum shall not go below 0.01 g^2/Hz. For components whose weight is greater than 182-kg or 400 pounds, the workmanship test spectrum is 0.01 g^2/Hz from 20 to 2000 Hz with an overall level of 4.4 g_{rms}.

Frequency (Hz)	ASD Level (g^2/Hz)
20	0.01
20-80	+3 dB/oct
80-500	0.04
500-2000	-3 dB/oct
2000	0.01
Overall	6.8 g_{rms}

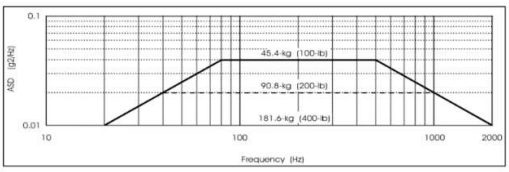

Figure 23. NASA General Environmental Verification Standard (GEVS)

Downloaded From: https://www.spiedigitallibrary.org/conference-proceedings-of-spie on 03 Dec 2021
Terms of Use: https://www.spiedigitallibrary.org/terms-of-use

To achieve reliable simulation results, a fine mesh is utilized in the analysis as shown in Figure 24. Global size of the elements is 3.00 mm with tolerance 0.15mm. Components that are complex and made of multiple materials were modeled as remote masses, attached to their mounting locations. No dampening was applied for the components modeled as remote masses. This ensures that the actual design's random vibration response would be better than the simulation results. The design is fixed at the payload tabs for the random vibration and launch analysis.

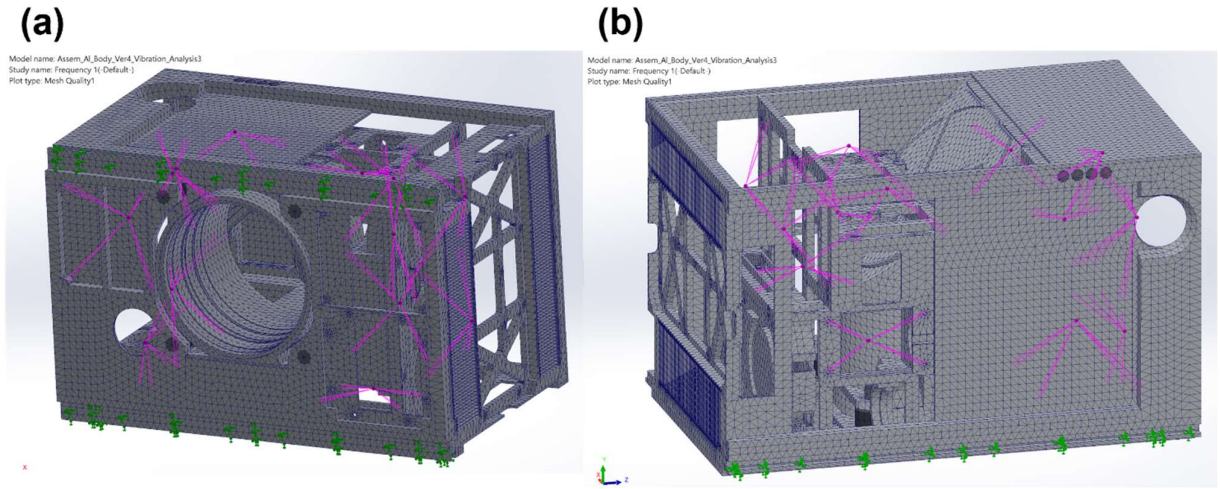

Figure 24. Vibration analysis (a)front view, (b) rearview.

To evaluate the effectiveness of the current design two cases were studied for the random vibration and launch simulation. Case A is the previous design and Case B is the current design that incorporates the novel shock and vibration control design.

4. 1. b. Modal Analysis

The modal analysis identified three dominant modes. Mode 1 in the z-direction at 368.63 Hz with 55% cumulative effective mass participation factor, Mode 2 in the x-direction at 509.53 Hz with 50.5% cumulative effective mass participation factor, and Mode 3 in the y-direction at 879.0 Hz with 60% cumulative effective mass participation factor. The dominant modes frequency plot can be seen in Figure 31, the Frequency vs. Cumulative effective mass participation plot can be seen in Figure 25, and Figure 26 shows visual plots of the three dominant modes. Also, the modes in each direction are illustrated in Figure 27.

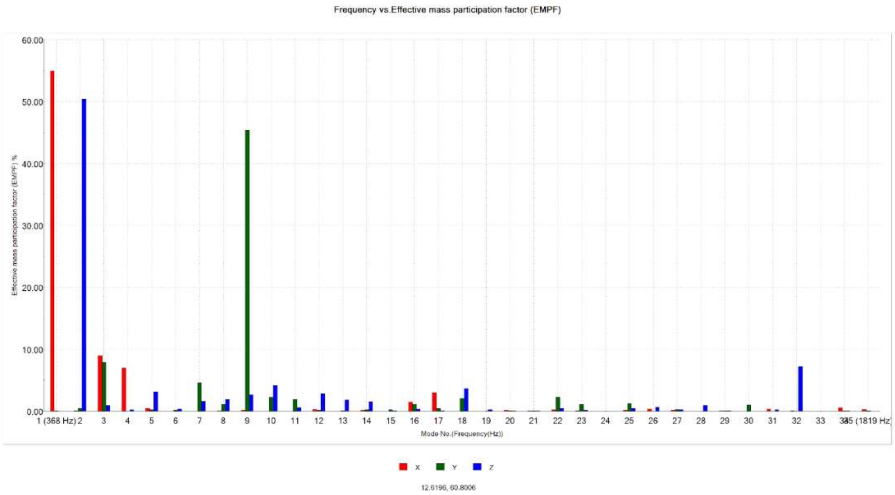

Figure 25. Frequency vs. effective mass participation factor

Downloaded From: https://www.spiedigitallibrary.org/conference-proceedings-of-spie on 03 Dec 2021
Terms of Use: https://www.spiedigitallibrary.org/terms-of-use

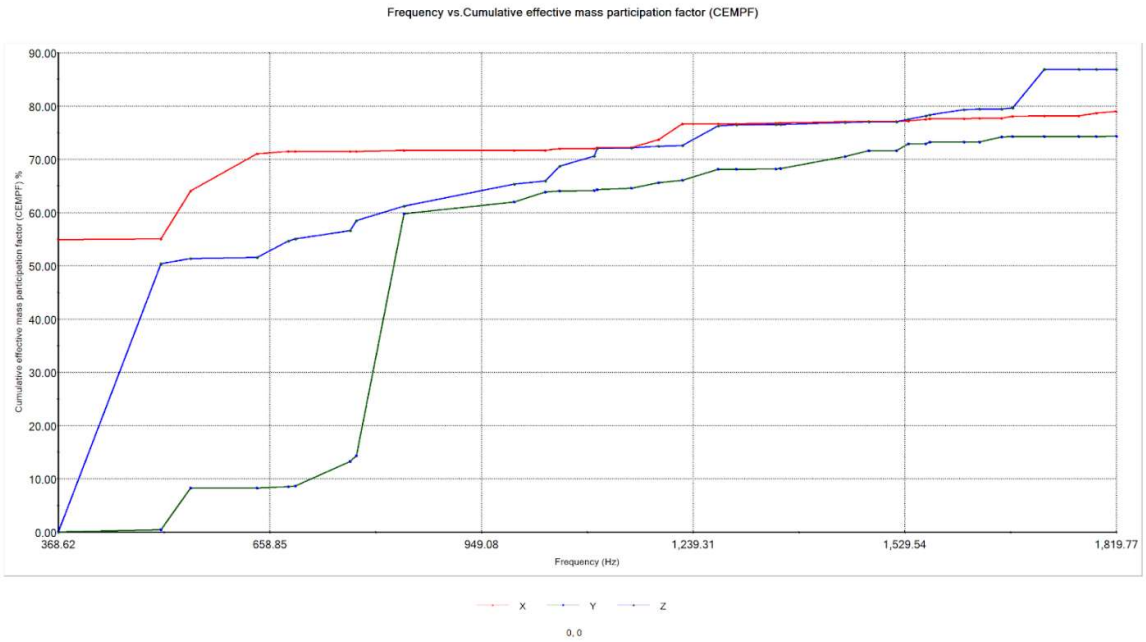

Figure 26. Frequency vs. cumulative effective mass participation factor

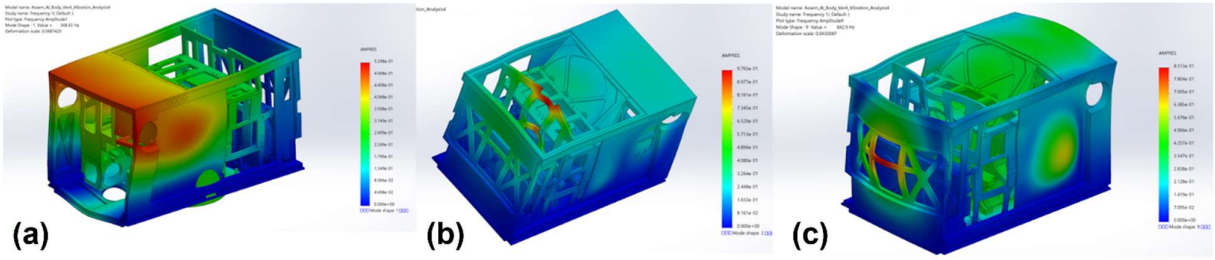

Figure 27. Modal analysis plot for the three dominant modes (a) Mode 1 (z-dir 368.63 Hz), (b) Mode 2 (x-dir 509.53 Hz), (c) Mode 3 (y-dir 879 Hz).

4. 1. c Random Vibration Analysis

The simulation yielded favorable results and it satisfied PSC's Dispenser System requirements, which require the maximum directional tab loading doesn't exceed 3559 N. NASA's guidelines for a spacecraft of 100 lbs or less were also satisfied. The following expression is used to calculate g_{rms} that indicate the 1σ acceleration response as $g_{rms} = \sqrt{0.5 \times \pi \times f_n \times Q \times ASD}$, where f_n is the natural frequency, Q stands for the quality factor and ASD is the acceleration spectral density at the corresponding frequency f_n with the unit g^2/Hz. The resulting directional RMS of quasi-static forces for 3σ is calculated by the following formula for each dominant mode and each direction as

$$Force\ (RSS) = g_{rms} \times Mass \times Cumulative\ Effective\ Mass\ Participation\ Factor \times 3 \qquad (1).$$

The computed results for each case and direction are tabulated in Table 3.

.

Downloaded From: https://www.spiedigitallibrary.org/conference-proceedings-of-spie on 03 Dec 2021
Terms of Use: https://www.spiedigitallibrary.org/terms-of-use

Table 3. Resulting directional RMS of quasi-static forces for 3σ

Direction	ASD [g^2/Hz]		Resulting 3σ [N]	
	Case A	Case B	Case A	Case B
X-Direction	42.45	42.20	1560	1646
Y-Direction	46.97	47.19	2007	1708
Z-Direction	56.91	58.30	2323	1902

The focus of the new design was not to improve the resulting directional RMS of quasi-static forces for 3σ but to isolate sensitive components from damage and misalignment. However, an improvement of the tab loading in the Y-Direction and the Z-Direction of 15% and 18% respectively. The experienced increase of 5.5% in the tab loading in the X-Direction is tolerable. In Figure 28, the displacement and strain for Case A and B are compared. Neither design experiences forces that are beyond the yield strength of the materials used.

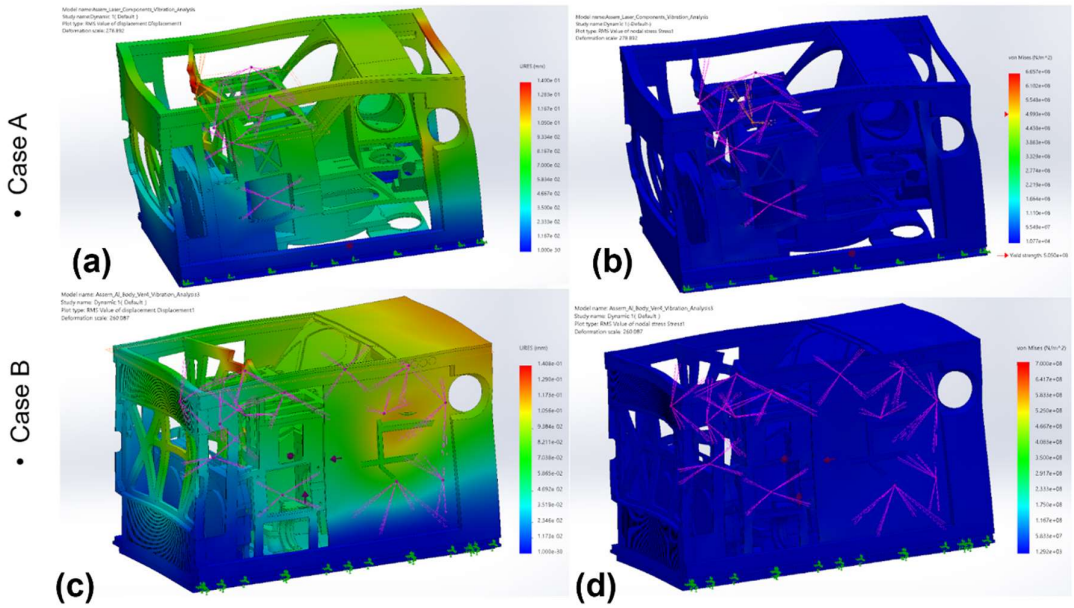

Figure 28. (a) Case A: random vibration displacement plot. (b) Case A: random vibration strain plot. (c) Case B: random vibration displacement plot. (d) Case B: Random Vibration Strain plot.

4. 1. d. Launch Analysis

Launch analysis followed NASA's General Environmental Verification Standard (GEVS) for spacecraft 100 lbs or less. The rocket that would be used to launch the CubeSat is currently unknown and a conservative approach needed to be taken. In order to cover the acceleration profiles of most rockets in use today, the acceleration profile of the Gemini-Titan VIII mission is used [14]. This particular rocket was chosen because the Titan rockets are modified Inter-Continental Ballistic Missiles (ICBMs) and are not designed for human comfort and their acceleration peaks above 7g. If the design can successfully survive the Titan rocket launch it will survive the launch of most rockets in use today. Modern rockets have much more forgiving peak acceleration.

Downloaded From: https://www.spiedigitallibrary.org/conference-proceedings-of-spie on 03 Dec 2021
Terms of Use: https://www.spiedigitallibrary.org/terms-of-use

To evaluate the benefits of the novel vibration and shock isolation design of the optical systems assembly, the launch simulation results of the previous and current designs are compared against each other. Case A is again the previous design version and Case B is the current design. Displacement simulation results show a significant improvement in the new design. The suspension effect of the new bottom plate design can be seen in Figure 29(c-d). The sturdy optical systems assembly bracket experiences significantly lower displacement values compared to Case A. The maximum displacement in Case A is 6.088×10^{-3} mm and in Case B is 5.011×10^{-7} mm. The simulation stress results also show significant improvement. Case A experiences 7.421×10^{6} N/m^2 maximum stress and Case B experiences 4.896×10^{2} N/m^2. As expected, the maximum stress is experienced by the bottom plate.

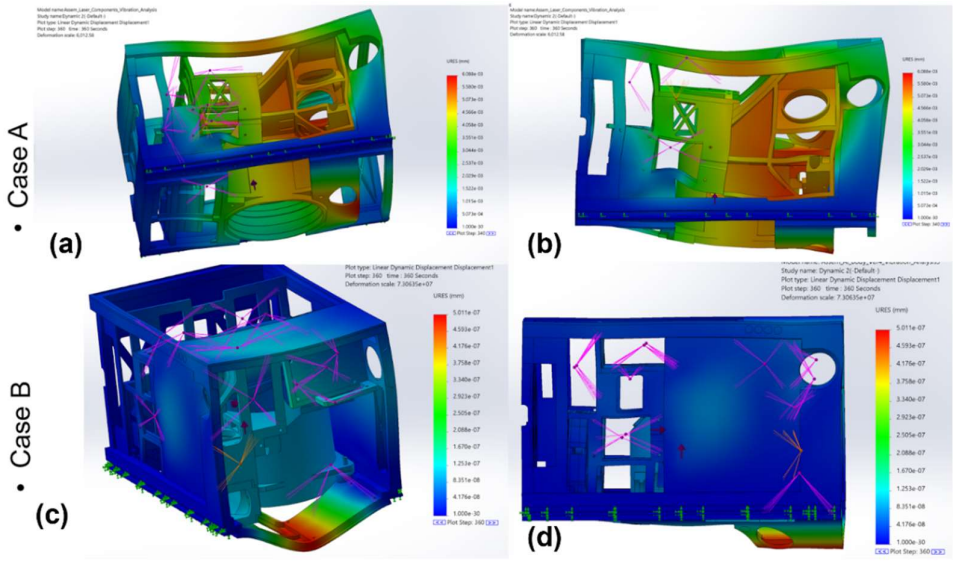

Figure 29. (a) Case A: launch simulation displacement front view. (b) Case A: launch simulation displacement side view. (c) Case B: launch simulation displacement front view. (d) Case B: launch simulation displacement side view.

The strain simulation results demonstrate the suspension function of the bottom plate and the dampening effect of the silicone rubber shock absorbers. The maximum strain is at the shock absorbers and it can be seen that the rest of the assembly. The strain simulation results for both cases with different views are presented in Figure 30.

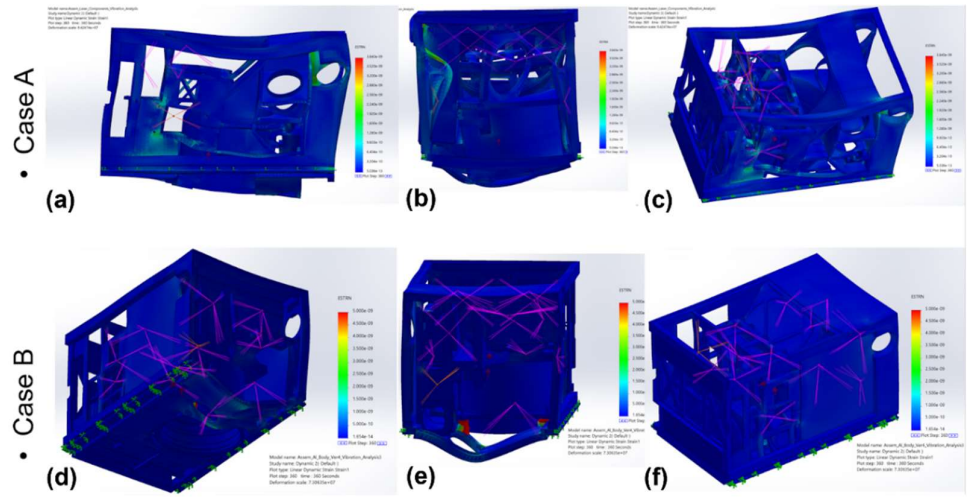

Figure 30. Case A: launch simulation strain plot for (a) bottom view, (b) rearview, and (c) side view. Case B: launch simulation strain plot for (d) bottom view, (e) rearview, and (f) side view.

Downloaded From: https://www.spiedigitallibrary.org/conference-proceedings-of-spie on 03 Dec 2021
Terms of Use: https://www.spiedigitallibrary.org/terms-of-use

The isolation of critical components in the optical systems assembly can be best seen in Figure 31, where the nodal stress at critical locations is compared. The stress experienced by the tabs, the bottom plate, and the fast-steering mirrors is plotted as a function of time.

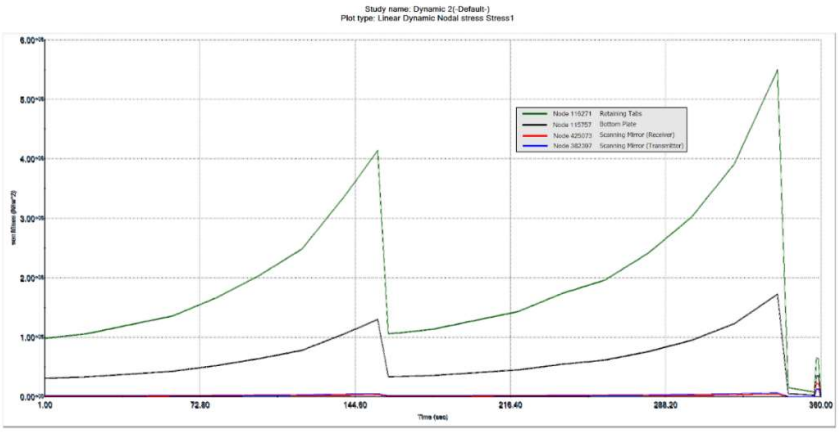

Figure 31. Nodal Stress response for the payload retaining tabs (green), the bottom plate (black), and the fast steering mirrors (red & blue).

4. 2. Thermal Analysis

Due to the presence of several high-power components, there are significant challenges in the thermal control systems design. One of the main difficulties encountered is to provide a thermal path from all components to the exterior radiating surfaces. In order to solve the issue, the material for the laser components mounting brackets is 7075-T651 like the rest of the satellite structural components. The brackets serve as thermal paths and as the satellite structural support. Another challenge is to maintain all of the components within their temperature operating ranges, which vary as can be seen in Table 4. To maintain the FPGA assembly and the signal laser assembly, heat pipes needed to be incorporated into the design. The FPGA heat pipe is clamped to the FPGA case and to the FPGA heat sink by a bracket and also clamped to the side radiators, ensuring good contact between. The signal laser has an integrated TEC and a heat pipe that is clamped to it and the side radiators, leading the excess heat to the exterior radiating surfaces. The pump lasers are the most challenging components for thermal control. Their heat generation rate is estimated to be 70W per laser. On top of being the top heat-generating contributors, the pump lasers need approximately 90 to 120 seconds to reach a steady-state before scanning. To solve this challenge two copper radiators, also serving as heat sinks, are mounted to the side plates and two TEC modules are sandwiched between the radiators and the pump lasers. This design allows the heat generated by the pump lasers to be pushed directly by the TECs to the radiators, minimizing the heat that reaches other temperature-sensitive components. The electronics assembly also utilizes a unique case and heat sink/radiator design that was previously described in detail. The thermal management components are illustrated in Figure 32.

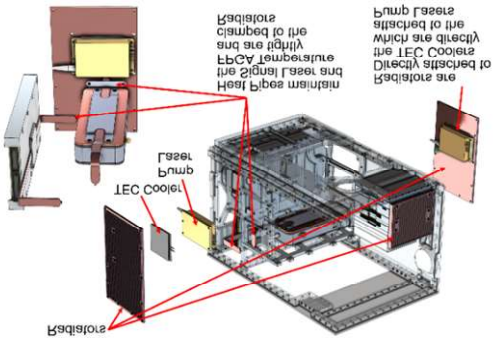

Figure 32. Thermal management systems overview

Downloaded From: https://www.spiedigitallibrary.org/conference-proceedings-of-spie on 03 Dec 2021
Terms of Use: https://www.spiedigitallibrary.org/terms-of-use

Table 4. Temperature operating range of critical design components

Component	Minimum Operating Temperature (°C)	Maximum Operating Temperature (°C)	Minimum Operating Temperature (K)	Maximum Operating Temperature (K)
Pump Laser	-20	70	253.15	343.15
Signal Laser	-10	50	263.15	323.15
Pre-Amp MAKO-AMP1064	-10	50	263.15	323.15
1064nm	-40	100	233.15	373.15
Beaglebone Black	-40	90	233.15	363.15
Pumpkin Space Batteries	-40	50	233.15	323.15
OBC Pumpkin	-45	85	228.15	358.15
X-band Module	-30	70	243.15	343.15
S-Band Module	-30	70	243.15	343.15
WDM	0	65	273.15	338.15
Pump Combiner	0	75	273.15	348.15
APD	-40	85	233.15	358.15
NIR-MX-LN-10 Modulator	0	70	273.15	343.15
Optimum Operating Range	0	50	273.15	323.15

4. 2.1 Methodology

A cold and a hot case were considered. The cold case represents the minimum temperature that the CubeSat would experience. The design had to be optimized so the temperature doesn't drop below the minimum operating temperature of the critical components. On the other hand, the hot case considers the highest experienced temperature regime and the concern is not to exceed the maximum operating temperature of the critical components.

The cold case would occur at BOL when the Thermal Tape (Silver Coated Teflon Thermal tape) is in perfect condition, offering the best reflectivity, and during the Vernal or Autumnal Equinox. The solar constant is about 1367W/m^2 and for Albedo effects the LEO Radiation Data from the CERES mission data was used which is also presented in Figure 33 [15]. For Earth's infrared radiation an average value of 250W/m^2 was used. On the other hand, the hot case would occur at the end of the life of the satellite when the thermal tape could have failed at places due to the atomic oxygen exposure, and during the winter solstice, when the satellite experiences maximum sun exposure due to the satellite orientation. The solar constant that is used is 1414 W/m^2 [16]. Albedo factor is taken from CERES LEO Radiation Data and used as in the cold case. The Earth's infrared radiation is again 250 W/m^2. The incident radiation on each side of the satellite was calculated using MATLAB and imported into SolidWorks Flow Simulation. Moreover, the parameters tabulated in Table 1 are considered for both hot and cold cases.

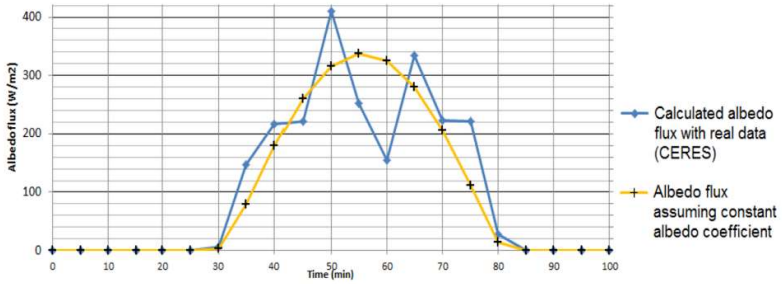

Figure 33. CERES Mission LEO albedo data

Downloaded From: https://www.spiedigitallibrary.org/conference-proceedings-of-spie on 03 Dec 2021
Terms of Use: https://www.spiedigitallibrary.org/terms-of-use

4.2.1 Cold Case Simulation Results and Analysis

During the cold case, the design is mostly focused on keeping all components above their minimum temperature ranges. The silver-coated Teflon thermal tape has been installed only on the top and front covers and portions of the bottom plate to prevent components from falling under the minimum required temperature. If it is installed on all applicable surfaces, certain components might fall below the required temperature.

The incident radiation plots in Figure 34 demonstrate the effects of the thermal tape when the top, bottom, and front sides are compared to the back, right, and left sides. Figure 35 shows the temperature variation over four orbits for the signal laser, the pump lasers, the FPGA assembly, the electronics assembly, and the bulk CubeSat body. All components stay within optimal operating range. The section view in Figure 36 shows the temperature distribution when the minimum temperatures occur and Figure 37 shows the transparency plot of the whole satellite with critical components highlighted. The main optics operating temperature plot during scanning is in Figure 38.

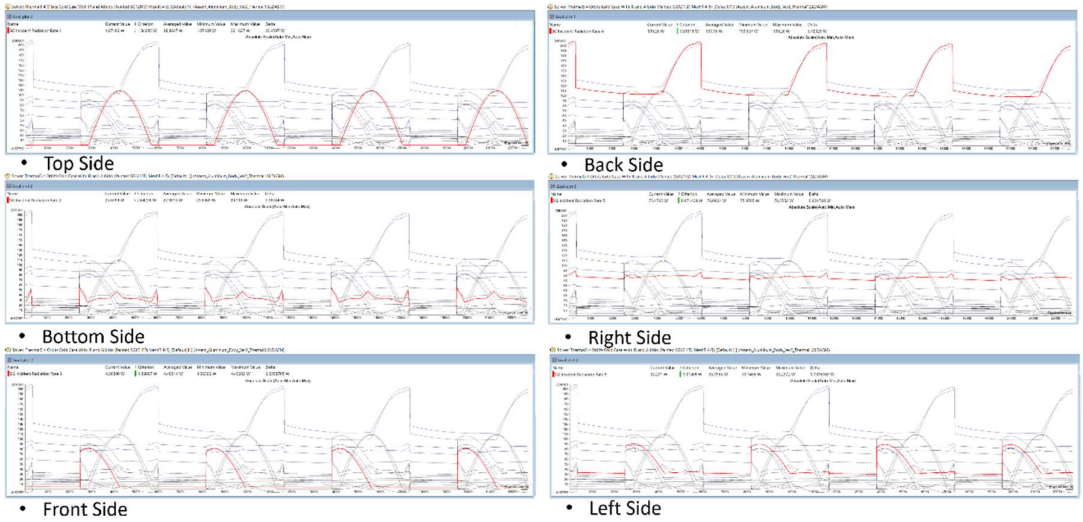

Figure 34. Incident radiation rate of the six sides of the CubeSat.

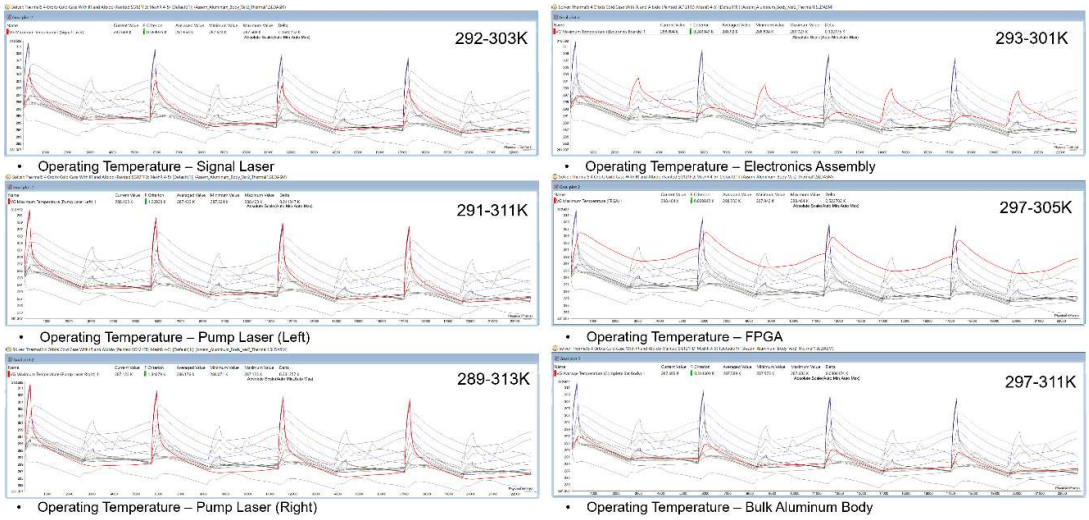

Figure 35. Cold Case: Temperature variation of critical design components over four orbits for critical components.

Downloaded From: https://www.spiedigitallibrary.org/conference-proceedings-of-spie on 03 Dec 2021
Terms of Use: https://www.spiedigitallibrary.org/terms-of-use

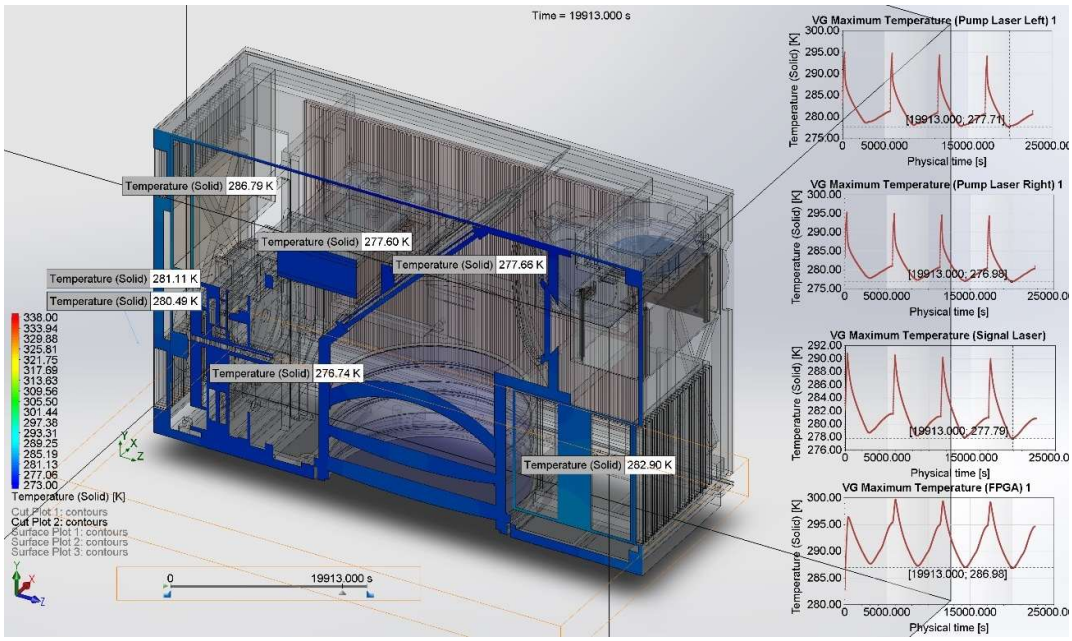

Figure 36. Cold Case: Lowest temperature section view.

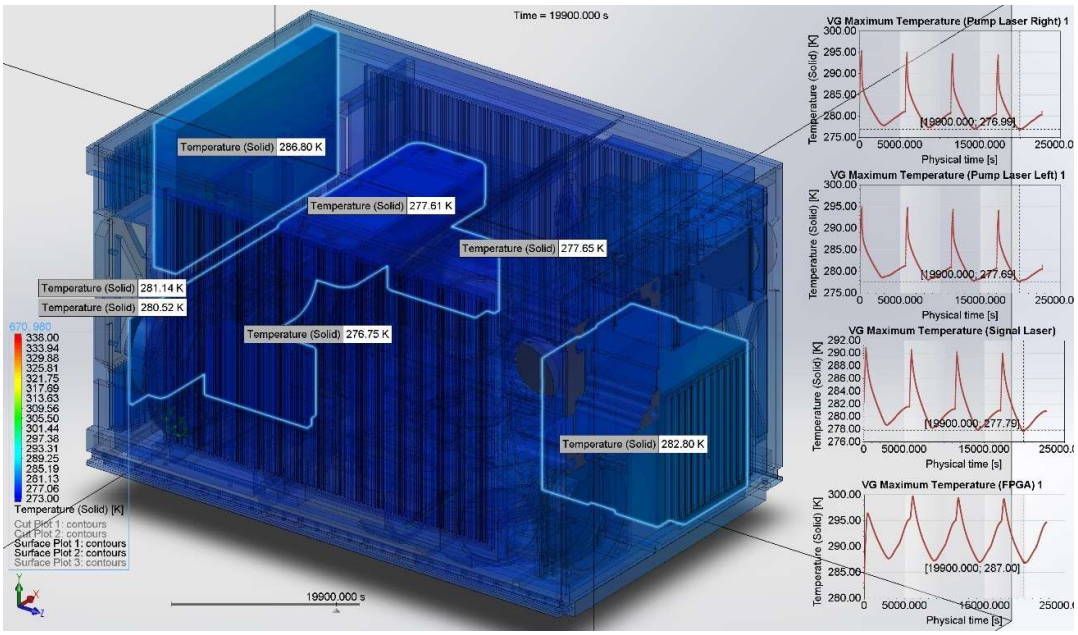

Figure 37. Cold Case: Lowest temperature transparency plot, where the critical components are highlighted.

Downloaded From: https://www.spiedigitallibrary.org/conference-proceedings-of-spie on 03 Dec 2021
Terms of Use: https://www.spiedigitallibrary.org/terms-of-use

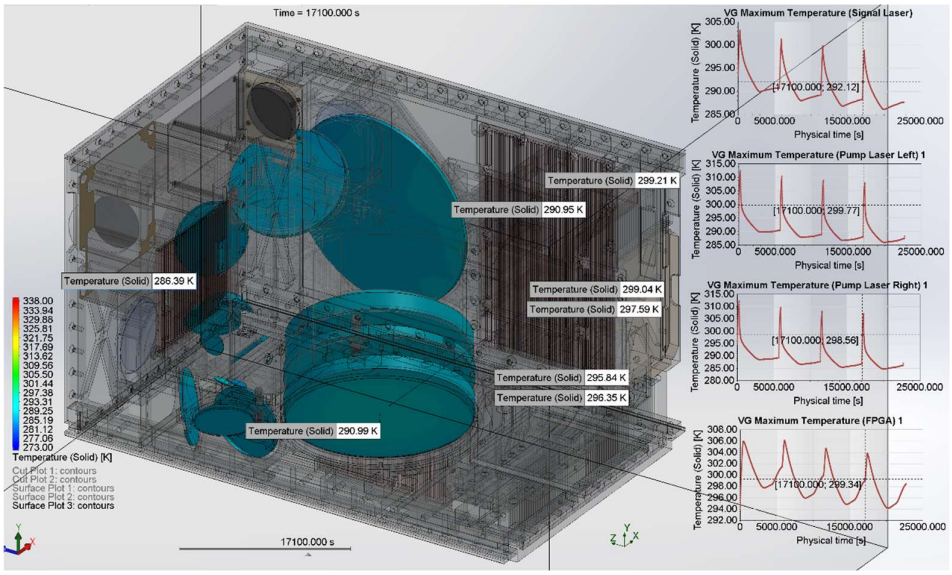

Figure 38. Cold Case: Optical components operating temperature

4.2.2 Hot Case Simulation Results and Analysis

During the hot case, the CubeSat design focuses on keeping the components below their maximum temperature ranges. If the silver-coated Teflon thermal tape has been installed on all surfaces, it would have been easier to solve the challenges of thermal control. However, heaters would have been required for some laser components, like the modulators and the pump combiners, and the power budget doesn't allow enough power during the cold case.

The incident radiation plots are in Figure 39 and Figure 40 shows the temperature variation over four orbits for the signal laser, the pump lasers, the FPGA assembly, the electronics assembly, and the bulk CubeSat body. None of the components exceeds the maximum temperature requirements. The section view shows the temperature distribution when the peak temperatures occur as in Figure 41 and Figure 42 shows the transparency plot of the whole satellite with critical components highlighted. The main optics operating temperature plot during hot case scanning is in Figure 43.

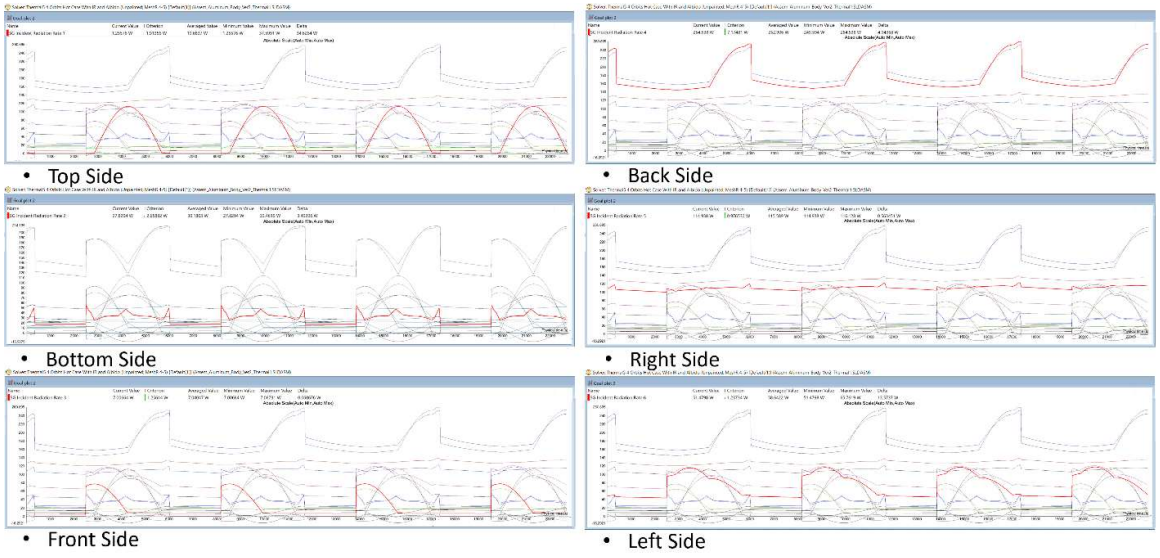

Figure 39. Hot Case: Optical components operating temperature over four cycles.

Downloaded From: https://www.spiedigitallibrary.org/conference-proceedings-of-spie on 03 Dec 2021
Terms of Use: https://www.spiedigitallibrary.org/terms-of-use

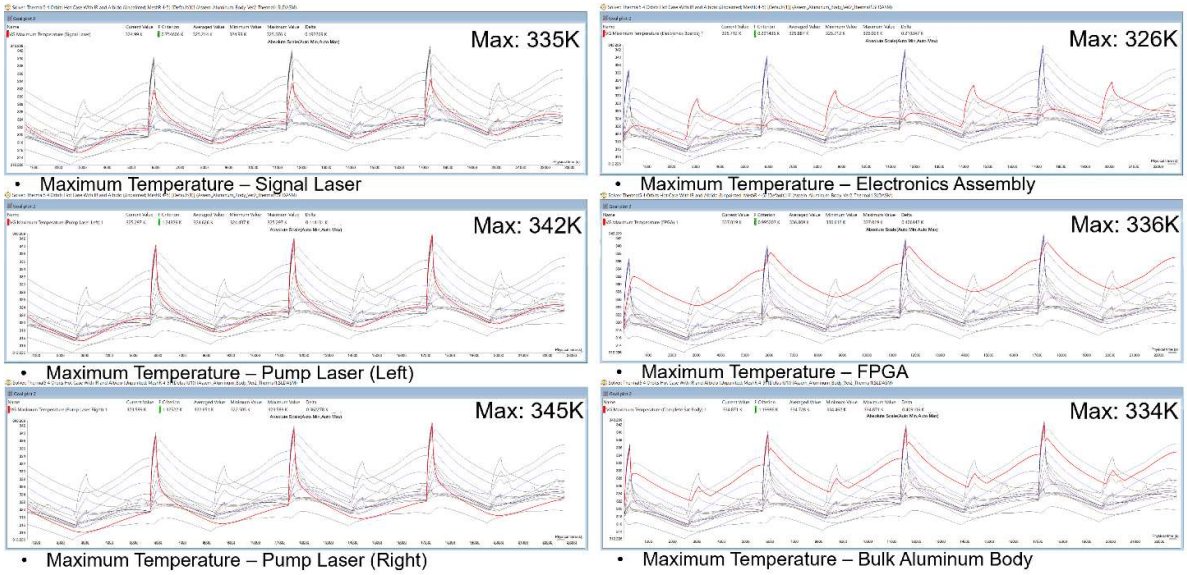

Figure 40. Hot Case: Optical components operating temperature over four cycles.

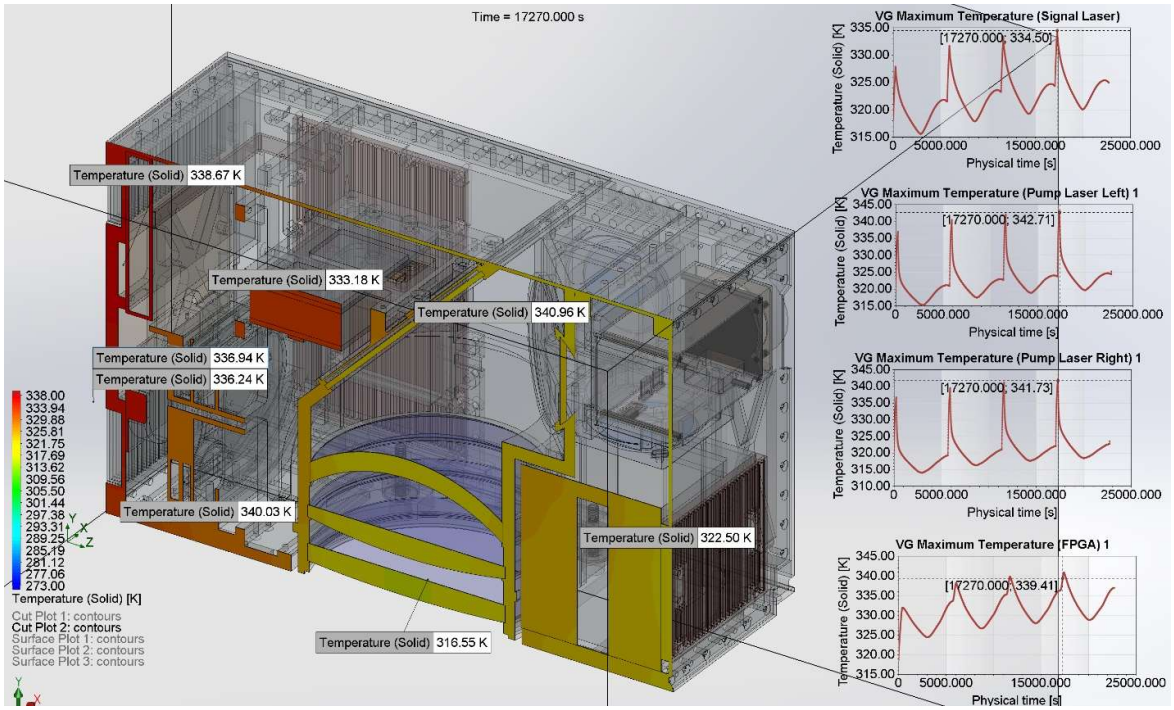

Figure 41. Hot Case: Highest temperature section view.

Downloaded From: https://www.spiedigitallibrary.org/conference-proceedings-of-spie on 03 Dec 2021
Terms of Use: https://www.spiedigitallibrary.org/terms-of-use

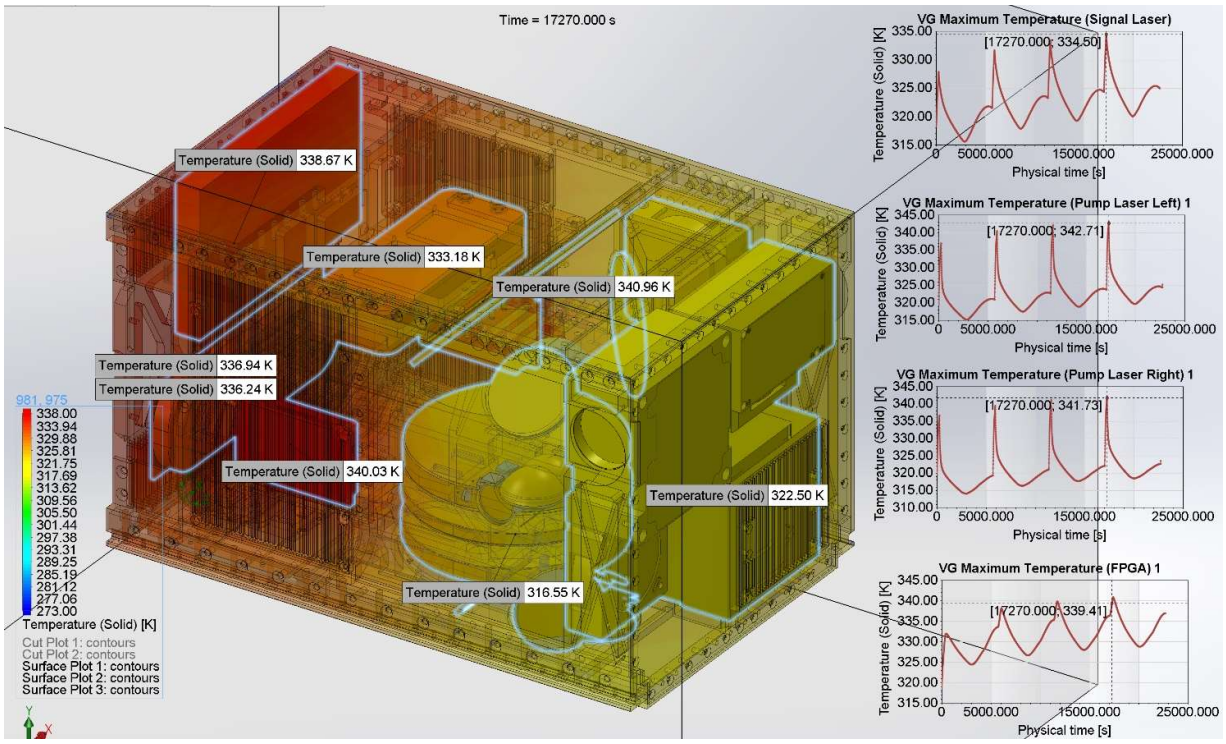

Figure 42. Hot Case: Highest temperature transparency plot with critical components highlighted.

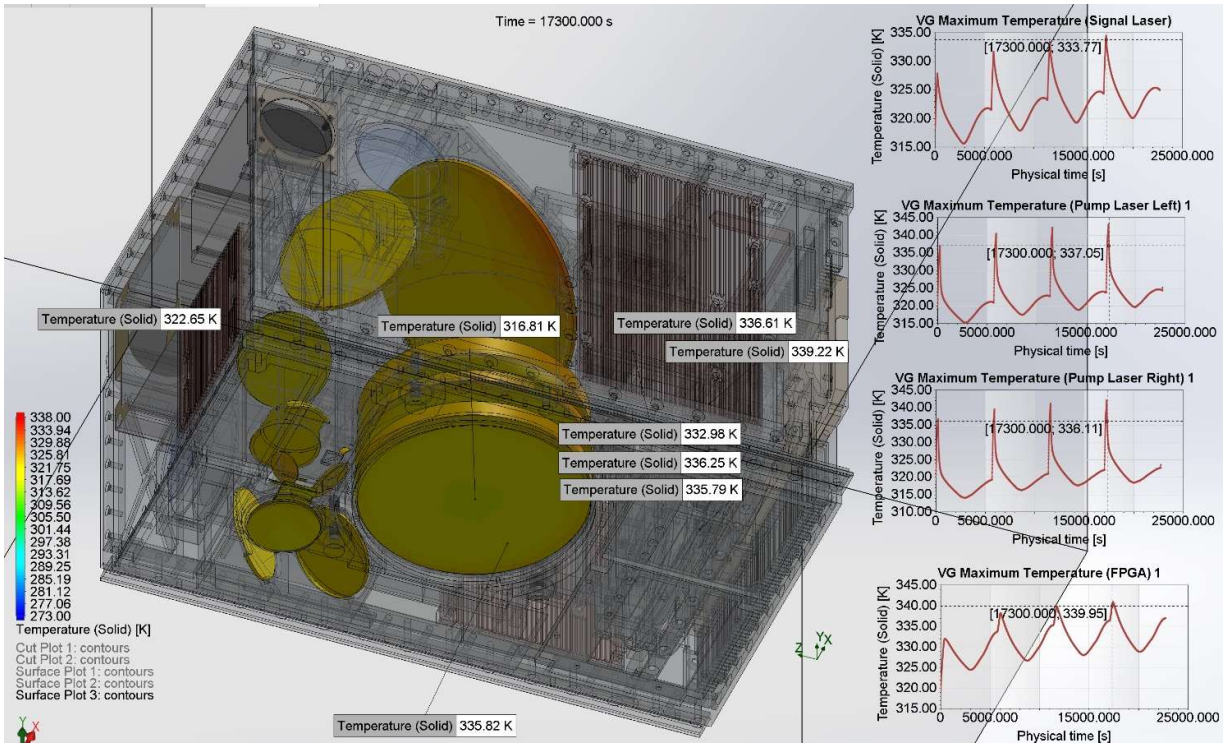

Figure 43. Hot Case: Optical components operating temperature.

Downloaded From: https://www.spiedigitallibrary.org/conference-proceedings-of-spie on 03 Dec 2021
Terms of Use: https://www.spiedigitallibrary.org/terms-of-use

5. CONCLUSION

We demonstrated the standalone CubeSat spacecraft technology that enables an optical remote sensing system for littoral ocean dynamics such as ocean surface height and wind vector with high optical power and pointing accuracy requirements. The designing and simulations were performed using SolidWorks, SolidWorks Simulation, SolidWorks Flow Simulation. The satellite utilized an integrated body design that serves as structural support for the payload and as a thermal path to the exterior radiating surfaces for the design's components. The innovative shock-absorbing body can handle the vibration and launch forces and isolate the critical optical components from damaging shock. The silicone shock absorbers can handle the low earth orbit environment and protect sensitive components. In terms of thermal control, the design is able to maintain all components within operating temperature ranges by utilizing active and passive systems. The novel side radiator/heat sinks design ensures the best possible cooling for the pump lasers, sandwiching the thermoelectric coolers between. This also limits the heat that is transferred to the rest of the CubeSat.

6. ACKNOWLEDGEMENTS

This work was supported by the Office of Naval Research under grant number # N00014-18-1-2845 and NASA Cooperative Agreement Partnerships with Universities (NNX16AT64A)

7. REFERENCES

[1] Erik Kulu, "Total nanosatellites and CubeSats launched", 4 April 2021, <https://www.nanosats.eu/img/fig/Nanosats_total_2021-04-04.pdf > (4 April 2021). Nanosats.eu

[2] Alicia Johnstone, "CubeSat Design Specification (1U – 12U) REV 14CP-CDS-R14", July 2020, <https://static1.squarespace.com/static/5418c831e4b0fa4ecac1bacd/t/5f24997b6deea10cc52bb016/1596234122437/CDS+REV14+2020-07-31+DRAFT.pdf> (July 2021). CubeSat.org

[3] ISIS Space Team, "16-Unit CubeSat structure", July 2021 <https://www.isispace.nl/product/16-unit-cubesat-structure/> (July 2021). Isispace.nl

[4] Planetary Systems Corporation Team, "Canisterized Satellite Dispenser", 3 Aug 2018, <https://www.planetarysystemscorp.com/wp-content/uploads/2014/07/2002337F-CSD-Data-Sheet.pdf> (3 Aug 2018). planetarysystemscorp.com

[5] Torun, R., Bayer, M.M., Zaman, I.U. and Boyraz, O., "Multi-tone modulated continuous-wave lidar," Proc. SPIE 10925, 109250V1-9 (2019).

[6] Torun, R., Bayer, M.M., Zaman, I.U., Velazco, J. E. and Boyraz, O., "Realization of Multitone Continuous Wave Lidar," 4, IEEE Photonics Journal **11**(4), 1–10 (2019).

[7] O. Boyraz, M. M. Bayer, R. Torun, and I. Zaman., "TuD2.2 - Multi Tone Continuous Wave Lidar (Invited)," IEEE Photonics Society Summer Topical Meeting Series (SUM), 1–2 (2019).

[8] Bayer, M. M., Torun, R., Li, X., Velazco, J. E. and Boyraz, O., "Simultaneous ranging and velocimetry with multi-tone continuous wave lidar," 12, Opt. Express **28**(12), 17241–17252 (2020).

[9] Bayer, M. M., Torun, R., Zaman, I. U. and Boyraz, O., "A Basic Approach for Speed Profiling of Alternating Targets with Photonic Doppler Velocimetry," Conference on Lasers and Electro-Optics, AW4K.4, Optical Society of America (2019).

[10] Bayer, M. M. and Boyraz, O., "Ranging and velocimetry measurements by phase-based MTCW lidar," Opt. Express **29**(9), 13552–13562 (2021).

[11] J. Rothka, R. Studd, K. Tate, and D. Timpe., "Outgassing of Silicone Elastomers," ARLON – Silicone Technology Division, Bear DE 19701, (2002).

[12] Planetary Systems Corporation Team, "Payload Specification for 3U, 6U AND 12U", Aug 2018, < https://www.planetarysystemscorp.com/wp-content/uploads/2018/08/2002367F-Payload-Spec-for-3U-6U-12U.pdf> (Aug 2018). planetarysystemscorp.com

[13] Nasa Goddard Space Flight Center Team, "GENERAL ENVIRONMENTAL VERIFICATION STANDARD (GEVS) For GSFC Flight Programs and Projects",28 March 2018, <https://explorers.larc.nasa.gov/2019APSMEX/MO/pdf_files/gsfc-std-7000a_final_3-28-18.pdf>, (28 March 2018). explorers.larc.nasa.gov

[14] Grimwood, J. M., " Project Gemini technology and operations - A chronology", NASA SP-4002, Wash., DC (1969).

Downloaded From: https://www.spiedigitallibrary.org/conference-proceedings-of-spie on 03 Dec 2021
Terms of Use: https://www.spiedigitallibrary.org/terms-of-use

[15] Rutan, D. A., S. Kato, D. R. Doelling, F. G. Rose, L. T. Nguyen, T. E. Caldwell, and N. G. Loeb, 2015: "CERES synoptic product: Methodology and validation of surface radiant flux". *J. Atmos. Oceanic Technol.*, **32**, 1121–1143 (2015).

[16] J. Meseguer, I. Perez-Grande, A Sanz-Andres, [Spacecraft Thermal Control] Woodhead Publishing in Meachanical Engineering, New York, 21-32 (2021).

Downloaded From: https://www.spiedigitallibrary.org/conference-proceedings-of-spie on 03 Dec 2021
Terms of Use: https://www.spiedigitallibrary.org/terms-of-use